



Optimizing in-situ monitoring for laser powder bed fusion process: Deciphering acoustic emission and sensor sensitivity with explainable machine learning

Vigneashwara Pandiyan^{a,*}, Rafał Wróbel^{a,b}, Christian Leinenbach^{a,c}, Sergey Shevchik^a

^a Empa, Swiss Federal Laboratories for Materials Science and Technology, Ueberlandstrasse 129, 8600 Dübendorf, Switzerland

^b ETH Zürich, Department of Materials, Laboratory for Nanometallurgy, Vladimir-Prelog-Weg 1–5/10, Zürich 8093, Switzerland

^c Laboratory for Photonic Materials and Characterization, École Polytechnique Fédérale de Lausanne, 1015 Lausanne, Switzerland

ARTICLE INFO

Keywords:

Laser Powder Bed Fusion
Process Monitoring
Empirical Mode Decomposition
Acoustic Emission
Explainable AI (XAI)

ABSTRACT

Metal-based Laser Powder Bed Fusion (LPBF) has made fabricating intricate components easier. Yet, assessing part quality is inefficient, relying on costly Computed Tomography (CT) scans or time-consuming destructive tests. Also, intermittent inspection of layers also hampers machine productivity. The Additive Manufacturing (AM) field explores real-time quality monitoring using sensor signatures and Machine Learning (ML) to tackle this. One such approach is sensing airborne Acoustic Emissions (AE) from process zone perturbations and comprehending flaw formation for monitoring the LPBF process. This study emphasizes the importance of selecting airborne AE sensors for accurately classifying LPBF dynamics in 316 L, utilizing a flat response sensor to capture AE's during three regimes: Lack of Fusion, conduction mode, and keyhole. To comprehensively understand AE from a broad process space, the data was collected for two different 316 L stainless steel powder distributions ($> 45 \mu\text{m}$ and $< 45 \mu\text{m}$) using two different parameter sets. Frequency analysis unveiled distinct LPBF dynamics as dominant and correlated in specific frequency ranges. Empirical Mode Decomposition was used to examine the periodicity of AE signals by separating them into constituent signals for comparison. Transformed AE signals were trained to distinguish regimes using ML classifiers (Convolutional Neural Networks, eXtreme Gradient Boosting, and Support Vector Machines). Sensitivity analysis using saliency maps and feature importance scores identified frequency information below 40 kHz relevant for decision-making. This study highlights interpretable machine learning's potential to identify critical frequency ranges for distinguishing LPBF regimes and underscores the importance of sensor selection for enhanced process monitoring.

1. Introduction

Laser Powder Bed Fusion (LPBF) is a rapidly developing Additive Manufacturing (AM) technique which is gaining popularity in various industries, including aerospace, automotive, and medical. By utilizing thermal energy as a laser beam, the LPBF process can selectively fuse specific regions of a replenishing powder bed, constructing a part layer by layer. This technique facilitates the creation of highly optimized designs, intricate lattices, and structures that were previously challenging or impossible to manufacture. In addition, the LPBF process allows for producing complex geometries in low-volume quantities, making it ideal for rapid prototyping or highly specialized applications. However, the interaction between the laser beam and the powder

particles during LPBF leads to various physics phenomena such as radiation absorption, instant melting, kinematics inside the melt pool, materials evaporation, solidification of material, and microstructure growth. These phenomena significantly depend on the parameters used during the LPBF process, including laser power, powder composition, scan speed and strategy, layer thickness, and environmental factors (DebRoy et al., 2018). If these parameters are not optimally set or if abrupt changes in environmental conditions occur, undesired mechanisms such as *balling*, *Lack of Fusion (LoF)*, crack propagation, delamination, and the formation of pores can occur (Snow et al., 2020). Therefore, controlling these parameters is critical to producing high-quality, defect-free LPBF components.

The LPBF process shows promise for metal-based manufacturing.

* Corresponding author.

E-mail address: vigneashwara.solairajapandiyan@empa.ch (V. Pandiyan).

<https://doi.org/10.1016/j.jmatprotec.2023.118144>

Received 28 May 2023; Received in revised form 26 August 2023; Accepted 3 September 2023

Available online 9 September 2023

0924-0136/© 2023 The Author(s). Published by Elsevier B.V. This is an open access article under the CC BY license (<http://creativecommons.org/licenses/by/4.0/>).

Still, ensuring that the produced parts meet quality standards is crucial, particularly in safety-critical applications such as biomedical and aerospace industries. There are two methods to quantify the components produced: post-mortem, which is the traditional approach, and in-situ, which is becoming more popular. Traditional post-mortem analyses such as X-ray tomography or ultrasounds are expensive and time-consuming. Furthermore, detecting defects in complex geometries through post-build imaging or mechanical testing is challenging. Also, the statistical quantification of defects for complex geometries is inappropriate because defects are not guaranteed to occur in repetitive locations. Other post-mortem quantification strategies, such as destructive testing, are time-consuming and expensive on customer-specific design modifications or small batch production sizes. Overall, the fundamental limitation of post-mortem assessment is its inability to rectify defects once they arise. This leads to unnecessary utilization of resources, including materials and machine time, on parts that will inevitably fail quality checks. Consequently, the popularity of in-situ monitoring is on the rise, offering real-time defect detection and the ability to adjust process parameters promptly. This can help to reduce the likelihood of producing defective parts, save time, and improve the overall quality of the final product. As a result, there is great excitement within the AM research communities for advancing real-time/in-situ quality estimation as a viable alternative to post-mortem. Recent progress in sensor technology and related signal processing methods, including Artificial Intelligence (AI) algorithms, has become instrumental in facilitating the development of in-situ quantification.

LPBF involves intricate laser-powder interactions and generates multiple events in the interaction zone. Therefore, it is vital to equip the process with sensors that can capture thermal, optical, and Acoustic Emissions (AEs) to monitor the process in real-time and gain a deeper understanding of it. The commonly used sensing technologies include pyrometers, high-speed cameras, Near-Infrared (NIR) spectrum thermography cameras, photodiodes, and AE sensors (Everton et al., 2016). Interpreting sensor data can provide insights into the process and identify undesirable mechanisms that need suppression. For instance, employing a high-speed camera enables monitoring of the shape and behavior of the melt pool (Kanko et al., 2016). By detecting defects such as porosity and *LoF* in real-time, adjustments can be made to process parameters to correct these issues. Additionally, infrared cameras can monitor build temperature (Zheng et al., 2019), identifying hotspots (Bartlett et al., 2018) and other temperature-related defects before they escalate into significant problems (Everton et al., 2016). Since the LPBF process and its mechanisms occur spontaneously, the sensor that is utilized for monitoring must possess a quick response time and be immune to dynamic changes (Mazzoleni et al., 2019). However, the visual and optical sensors used for monitoring LPBF encounter difficulties due to the small dimensions of the melt pool, 50–250 μm , which are visible only for a few microseconds, leading to challenges in achieving spatial and temporal resolution (Cheng et al., 2017). Furthermore, plumes and vapours obstruct the visibility of the process zone, and the processing of high-speed imaging data streams is computationally demanding. Alternatively, AE sensors are a reliable and cost-effective option as they can sense volumetric information from the material bulk and have a high temporal resolution, making them suitable for monitoring melt pool occurrences in the 10–100 μs time scale (Khairallah et al., 2016). Despite requiring fewer computational resources for processing data, installing AE sensors requires caution because of the 3D nature of acoustic waves, which affects their sensitivity and signal strength. However, AE sensors can be installed with minimal modifications to existing machinery and are more cost-effective than visual and optical sensors. For industrial and commercial applications of AE sensing in LPBF, it is essential to carefully consider sensor location, distance, angle, and filtering to ensure optimal sensitivity and signal strength.

(Redding et al., 2018) proposed a non-destructive airborne acoustic inspection method that captures acoustic pressure waves emanating from the process zone in LPBF without attaching sensors beneath the

build substrate. The sources of acoustic pressure waves in LPBF can be classified into three main categories: thermal-mechanical sources, powder bed interactions, and laser-material interactions. Thermal-mechanical sources result from the thermal expansion and contraction of the metal powders and the melting and solidification of the metal. Powder bed interactions-based sources include spattering, erosion, denudation, and sintering of the metal powders, while laser-material interactions include melt pool perturbations due to the absorption, reflection, and transmission of the laser beam by the metal powders and the solidified metal. Various types of AE sensors that work on different principles, such as condenser (Chen et al., 2023), dynamic (Pandiyan et al., 2021), piezoelectric (Kononenko et al., 2023), electret (Harake, 2022), fiber Bragg grating (Shevchik et al., 2018), and laser-based (Gutknecht et al., 2021) to convert the acoustic pressure waves to a digitalized temporal waveform, have been reported for process monitoring in LPBF. Grasping the patterns in the multifaceted AE waveforms extracted from the LPBF process zone can aid in characterizing the underlying physics of these mechanisms and constructing an inclusive monitoring system with high reliability. Nevertheless, the ever-changing interaction between lasers and materials creates pressure waves that are difficult for human operators to decipher and make quick decisions on (Pandiyan et al., 2020). However, by combining signal processing and machine learning (ML), more valuable insights can be gained compared to traditional methods. This can lead to better decision-making for process monitoring and optimization, including the ability to model the system's behaviour, detect defects or anomalies, and predict potential issues before they arise. Ultimately, this results in a more dependable and effective monitoring system.

(Ito et al., 2021) showed that the microcrack generated during LPBF in real-time can be detected by continuously recording and wirelessly transmitting AE waveforms. Acoustic emission was used to detect *LoF* and *balling* effect in single tracks simulated with increased powder layer thickness. Due to complexity, AE signals recorded during processing have been analyzed with wavelets (Pandiyan et al., 2020), frequency (Drissi-Daoudi et al., 2022), and Short-time Fourier transforms (Kouprianoff et al., 2018). Spatial and temporal localization of pores was achieved by analyzing the recorded time series of laser position and acoustic pressure using Ensemble Empirical Mode Decomposition (EMD), traditional Fourier decomposition, and statistical measures (Tempelman et al., 2022a). Specific partitions of the acoustic signals corresponding to *keyhole pore* formation were identified using signal processing and ML techniques. Signal processing techniques and ML algorithms can extract valuable information from the complex AE data streams generated during the LPBF process (Tempelman et al., 2022b). A defect detection system that utilizes a deep belief network (DBN) and microphone data has been reported to categorize *balling* and other mechanisms (Ye et al., 2018a). (Luo et al., 2021) proposed a deep learning algorithm to monitor spatter using a microphone by establishing the correlation between acoustic signals and spatter captured by a high-speed camera. (Shevchik et al., 2018) developed a Deep Convolutional Neural Network (D-CNN) that accurately classified porosity content in the LPBF process using wavelet spectrograms obtained from acoustic signals collected via a fiber Bragg grating. Also, (Shevchik et al., 2019) proposed a CNN network that utilized two input-running windows composed of long and short wavelet spectrograms to process and analyze AE signals for quality monitoring. (Ye et al., 2018b) demonstrated a defect-recognition technique for detecting five different process conditions in single tracks fabricated by 304 L stainless steel powder. The approach involved utilizing support vector machines (SVM) and statistical features extracted from recorded microphone signals. In their earlier studies, the authors suggested a semi-supervised approach to differentiate between anomaly regimes (such as *balling*, *LoF*, and *keyhole*) and AE signatures of the defect-free regime (Pandiyan et al., 2021). This approach involved training a generative model based on a variation autoencoder and Generative Adversarial Network (GAN) using only the distribution of the AE dataset corresponding to the defect-free

regime. (Pandiyan et al., 2022a) demonstrated that transfer learning could be effectively employed between materials by utilizing two network architectures initially trained for classification using spectrograms representing LPBF mechanisms. (Li et al., 2022) combined Airborne AE signals captured using a microphone and photodiode signals obtained from the process zone to train a CNN model to extract and fuse the features derived from both sensor's for in-situ quality monitoring in LPBF.

(Goh et al., 2021) showed that the application of intelligent monitoring in AM has increased due to the advancement of ML algorithms. As ML algorithms continue to develop, we can expect even more advanced applications in the process monitoring of AM in the future. In-situ monitoring is still a developing technology, but it will likely become more common as LPBF gains popularity in various industries. The complexity of ML algorithms depends on the patterns in the sensor data, and most research has focused on treating AE data with state-of-the-art ML algorithms. Literature has reported that airborne AE sensors have varying sensitivity ranges, such as 40 Hz to 15 kHz (Bevans et al., 2023), 4 Hz to 20 kHz (Kouprianoff et al., 2018), 39–42 kHz (Pandiyan et al., 2022a), 3.15–51.2 kHz (Luo et al., 2021), 3.15 Hz to 20 kHz (Zhirnov et al., 2022) and low sensitivity below 50 kHz (Gutknecht et al., 2021), but they have successfully monitored AM process when used in conjunction with ML. Previous research has overlooked the comprehensive enhancement of AE information collected from the process zone perturbations, particularly with the sensor's efficacy in capturing vital information essential for informed decision-making. This study aims to bridge this gap by evaluating the ML model's complexity with the AE sensor information and proposes a framework for effective sensor selection based on the nature of AE emissions from the process zone. This study goes beyond traditional ML classification methods and spotlights the crucial role of sensor selection in refining the accuracy for classifying LPBF regimes. It delves into frequency ranges that clearly distinguish the boundaries between these conditions, intending to establish a robust approach for selecting sensor ranges that enhances classification accuracy. Unlike prior investigations, this study specifically explores the impact of utilizing airborne AE sensors sensitive to LPBF dynamics in 316 L on the accuracy of LPBF regime classification. The study meticulously compares AE signals corresponding to different conditions and then trains ML classifiers, namely CNN, eXtreme Gradient Boosting (XGBoost), and SVM, on the transformed AE signals to differentiate these conditions effectively. Subsequently, the trained models are subjected to sensitivity analysis using saliency maps and feature importance scores, obtained through permutation and SHapley Additive exPlanations (SHAP), to identify the frequency range information critical for informed decision-making. Notably, the study emphasizes the potential of an interpretable machine learning framework in identifying pivotal frequency ranges for distinguishing LPBF regimes beyond the scope of process monitoring.

This paper is organized into five sections. Section 1 presents a concise outline of the LPBF process and the research gap that will be addressed in this work. The LPBF experimental setup, customized in-situ monitoring setup, powder characterization findings and dataset collections are all presented in Section 2. Section 3 compares the AE signals' spectrum and temporal feature distributions from laser-material interaction from different process spaces using periodogram and EMD analysis. Additionally, the predictions made by the CNN, XGboost and SVM based on AE data corresponding to four datasets and the saliency and feature importance score mapped with frequency range in AE signal are reported. Finally, the findings of this paper and the future directions on in situ monitoring for the LPBF process are summarized in Sections 4 and 5.

2. Materials and methods

2.1. Experimental setup

The LPBF experimental setup consisted of a SISMA MySint 100 LPBF machine equipped with a fiber laser operating at 1070 nm wavelength, producing a Gaussian laser spot with a $1/e^2$ diameter of 55 μm . The build chamber utilized argon gas at atmospheric pressure to create an inert environment. The Raleigh range of the laser beam was approximately 2.15 mm. These parameters collectively formed the foundation for the conducted LPBF experiments. Furthermore, a customized in-situ AE sensing system was installed within the processing chamber, as depicted in Fig. 1.

The in-situ system developed for LPBF monitoring in this research includes a CM16/CPMA (Avisoft Bioacoustics, see Fig. 2(a)) airborne AE sensor, which has a frequency response range of 0–150 kHz as shown in Fig. 2(b). To ensure the sensitivity of the AE sensor, as illustrated via Fig. 2(c) in the form of a polar pattern plot, a specialized fixture is employed to securely position the supercardioid sensor with its sensing side oriented towards the build plate. The sensor's diaphragm is positioned in close proximity, approximately 12 cm away, and set at a 45-degree angle directed towards the process zone. Additionally, an extra precautionary measure has been integrated. This involves utilizing a bronze mesh supplied by the manufacturer to shield the sensor's diaphragm. This mesh acts as a physical barrier, effectively safeguarding the sensor's diaphragm against direct exposure to any potential splatter or particulate matter that could be emitted during the process zone. The choice of the sensor in this study is critical for detecting all process zone perturbations and verifying the proposed signal processing methods. In contrast to the airborne acoustic sensors used on AM process monitoring in earlier studies that primarily relied on detecting waveforms within specific frequency ranges—such as 40 Hz to 15 kHz (Bevans et al., 2023), 4 Hz to 20 kHz (Kouprianoff et al., 2018), 39–42 kHz (Pandiyan et al., 2020), 3.15–51.2 kHz (Luo et al., 2021), 3.15 Hz to 20 kHz (Zhirnov et al., 2022)—and differing from acoustic sensors employed in earlier investigations that exhibited insufficient sensitivity in the lower-frequency range below 50 kHz when addressing repairs for keyhole porosity (de Formanoir et al., 2023), as well as in understanding the dynamics of remelting under pulsed laser conditions (Nasab et al., 2023), and assessing AE with other optical sensing techniques (Gutknecht et al., 2021), the chosen sensor for this research offers distinct advantages. It has a flat frequency response over an extended range, as depicted in Fig. 2(b), eliminates bias and amplifies its sensitivity across a broader spectrum, making it suited for the proposed signal processing techniques and is essential to ensure the validity and effectiveness of the methods.

The schematic representation in Fig. 3 visually outlines the AE data acquisition pipeline used in the work. The first channel of the Data Acquisition (DAQ) is dedicated to capturing optical emissions from laser-powder bed interactions, while the second channel is designated for acquiring acoustic data. The trigger for initiating the data acquisition was based on the optical channel obtained when the laser interacted with the powder bed. A fixed focus collimator of the F220SMA-980 type (Thorlabs) is positioned off-axial to capture optical signals from the interaction region. The optical signals are then directed to the photodiode (PDA20CS2, 800–1700 nm; Thorlabs) through a fiber patch cable with a core diameter of 550 μm . The photodiode transforms the optical signals into an analog voltage signal proportional to the intensity the detector absorbs. Once this voltage signal exceeds a predetermined threshold (0.5 V in our case), it triggers the DAQ card to commence the acquisition of two channels. The photodiode and AE sensor signals are acquired simultaneously using an Advantech 1840 PCIe data acquisition card (Advantech, USA), with a dynamic range of ± 5 V and a sampling rate of 400 kHz. The data acquisition rate was selected to ensure that the frequency response of the AE sensor complies with the Nyquist-Shannon theorem (Jerri, 1977). The optical and AE channels are synchronized,

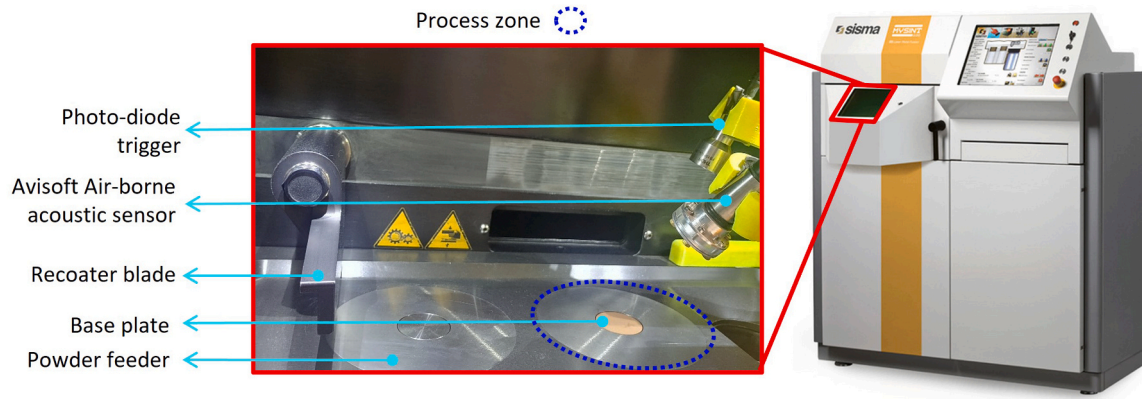


Fig. 1. Sisma MYSINT 100 augmented with airborne acoustic sensor and photodiode trigger for LPBF process.

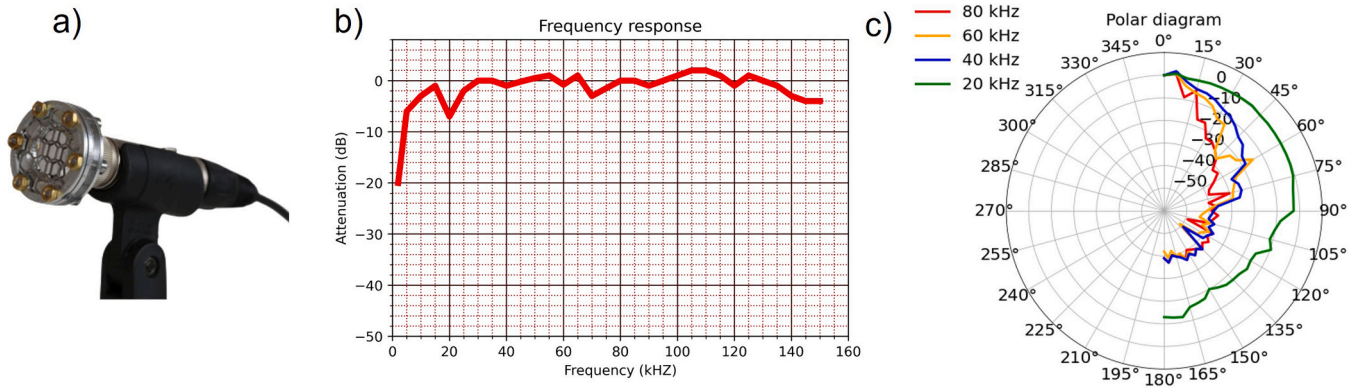


Fig. 2. a) Avisoft bioacoustics CM16/CPA airborne AE sensor equipped with a bronze mesh, b) Frequency response of the sensor, c) Polar diagram of the sensor.

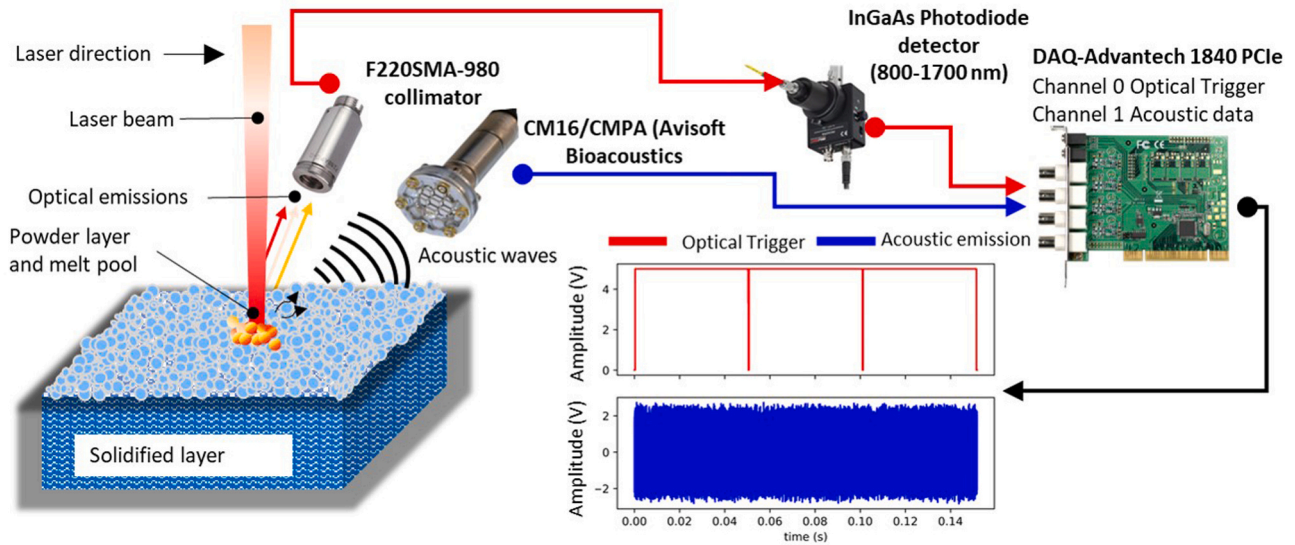


Fig. 3. Schematics of the proposed sensing system comprising photodiode and AE sensors.

and the photodiode gain is preconfigured to achieve an intensity exceeding the upper saturation limit 5 V with each laser exposure to the powder bed, resulting in a square wave. The AE signatures obtained in this square wave window correspond to each scan track and can be processed subsequently.

2.2. Materials

In this study, the feedstock material used was gas-atomized 316 L stainless steel powder obtained from Oerlikon Metco in Switzerland. The powder was spherical primarily, with an initial particle size distribution ranging from 15 μm to 60 μm . Two different particle size distributions were obtained from the gas-atomized 316 L stainless steel powder used

in this study. This was achieved by using a vibrating sieve with a mesh size of 325 (45 μm distance between wires) to obtain two distributions, *P1* (consisting of particles in the upper range of the sieved distribution) and *P2* (consisting of particles with diameters < 45 μm). By generating two different powder size distributions, the study aimed to investigate the acoustic spectra emitted on a wider processing space as the powder interacts with the laser source. Specifically, the study aimed to understand how changes in particle size distribution, scanning speed and laser power affect the AE's generated during the powder-bed fusion process.

Distributions of the 316 L powder particles corresponding to *P1* and *P2* were measured using the Mastersizer 3000® (Malvern, UK) particle size analyzer based on the laser diffraction technique, as shown in Fig. 4. Comparing the two distributions in Fig. 4 reveals that *P1* has most particle sizes centred around 40 μm with only a small fraction of particles < 20 μm . In contrast, *P2* has a significant amount of finer particles, less than 40 μm . Table 1 displays the statistical particle size distribution for the two distributions (*P1* and *P2*) in terms of *D10*, *D50*, and *D90* metrics. These metrics are noticeably distinct for each distribution. This characterization suggests that any differences in the acoustic signatures from the process zone could directly correlate to the different particle size distributions.

2.3. Process parameters

We fabricated two cuboids (A and B) samples measuring 20 mm in width and length from two powder distribution batches - *P1* and *P2*. Different combinations of laser power and scanning speed were used to realize three LPBF regimes: *LoF*, *conduction mode* and *keyhole*, as indicated in Table 2. Two sets of the three LPBF regimes were induced in each cuboid built with one of the powder distributions. To understand the acoustic signals produced from the process zone, two laser power parameters with minor offsets were employed to induce each of the three LPBF regimes in each cuboid resulting in four datasets - *D1*, *D2*, *D3* and *D4*. The experiments were carried out in an argon gas environment with less than 0.1% oxygen. All two cuboids were fabricated using the following sequence of regimes (from bottom to top): two sets of the *keyhole*, two sets of *conduction*, and two sets of *LoF* regimes in each cube after the initial "build-up" phase. This particular order was chosen to prevent any artifacts from the previous regimes from influencing the acoustic signature of the current regime. A bidirectional scanning approach was used, with a 90° rotation between layers, a layer thickness of 30 μm and a hatch distance of 0.1 mm for all three processing regimes of the two powder fractions. Typically, the powder layer is thicker prior to laser irradiation than the powder particles that combine to form a dense layer as the cavity is filled. Consequently, after the powder bed is refreshed, the cavity of the new layer is thicker than the maintained layer thickness (Wischeropp et al., 2019). Therefore, even though a layer thickness of 30 μm is maintained, particles from distributions *P1* and *P2*

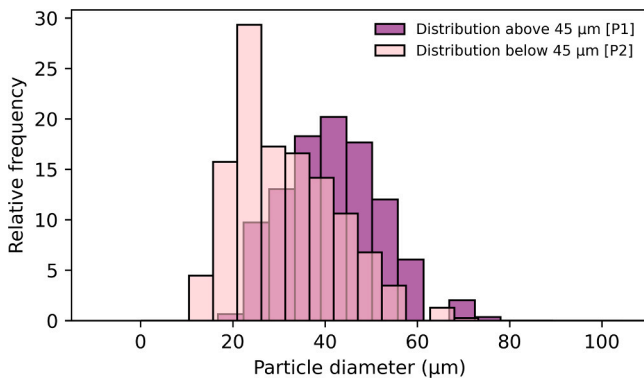


Fig. 4. Particle size distribution in the two 316 L powders *P1* and *P2* used in the study.

Table 1

Statistics of cumulative particle size distribution in terms of *D10*, *D50* and *D90*.

| Category | <i>D10</i> | <i>D50</i> | <i>D90</i> |
|--|--------------------|--------------------|--------------------|
| Particle distribution above 45 μm [<i>P1</i>] | 30.9 μm | 42.3 μm | 57.9 μm |
| Particle distribution below 45 μm [<i>P2</i>] | 19.1 μm | 29.6 μm | 45.3 μm |

Table 2

LPBF process parameters on the two different powder distributions.

| | Laser Power (W) | Scan speed (mm/s) | Particle distribution above 45 μm [<i>P1</i>] | Particle distribution below 45 μm [<i>P2</i>] |
|-----------------|-----------------|-------------------|--|--|
| Lack of Fusion | 110 | 800 | Dataset [<i>D1</i>] | Dataset [<i>D3</i>] |
| Conduction mode | 160 | 400 | | |
| Keyhole | 160 | 75 | | |
| Lack of Fusion | 90 | 800 | Dataset [<i>D2</i>] | Dataset [<i>D4</i>] |
| Conduction mode | 140 | 400 | | |
| Keyhole | 180 | 75 | | |

greater than 45 μm in size could be accommodated. Labelling the three regimes used in the four AE datasets is based on the process parameters corresponding to induce them. Furthermore, the existence of the regimes was confirmed using an optical micrograph.

To verify the existence of the three LPBF regimes, cuboid cross-sections were analyzed using optical microscopy. These sections were cut perpendicular to the scan tracks and then ground and polished in accordance with metallographic preparation standards. As depicted in Fig. 5, the varying levels of build density, porosity, and voids observed across each regime confirmed that the selected laser powers and scanning speeds led to the intended regimes for the two cuboids, which were printed using two different particle size distributions. The primary goal of contemporary manufacturing is to create flawlessly dense parts without defects. The *conduction mode* fits well with this objective. Nevertheless, it is essential to recognize that while the *conduction mode* is ideal for defect-free parts, a holistic grasp of all LPBF regimes and dynamics is essential for process monitoring and quality control. Manufacturers can customize process parameters, identify variations, and uphold rigorous quality control by comprehending the sensor signature dynamics across these regimes.

2.4. Dataset preparation

During the fabrication of the cube using bidirectional scanning, data acquisition for both optical and acoustic channels is initiated for each layer as soon as the optical signal detected by the photodiode crosses the threshold of 0.5 V at the layer's outset. The photodiode detector gain was preset to ensure an intensity surpassing the upper saturation limit of + 5 V. Each instance of laser exposure to the powder bed on each scan track in a layer generates a square wave pattern. In the case of layers containing bidirectional scan tracks, the count of square waves corresponds directly to the quantity of scan tracks present within each layer. The synchronization of the optical and AE channels enables the extraction of a dataset comprising AE windows with a 12.5 ms time scale in each scan track. The AE signals that are chopped into a 12.5 ms window (5000 data points) are subjected to offline low-pass Butterworth filtering with a cut-off frequency of 150 kHz, based on the frequency response specification of the AE sensor, irrespective of the regime and cube. For more information on the AE dataset used in this study, please refer to Table 3. The data preparation strategy was the same for the four datasets, each consisting of three regimes.

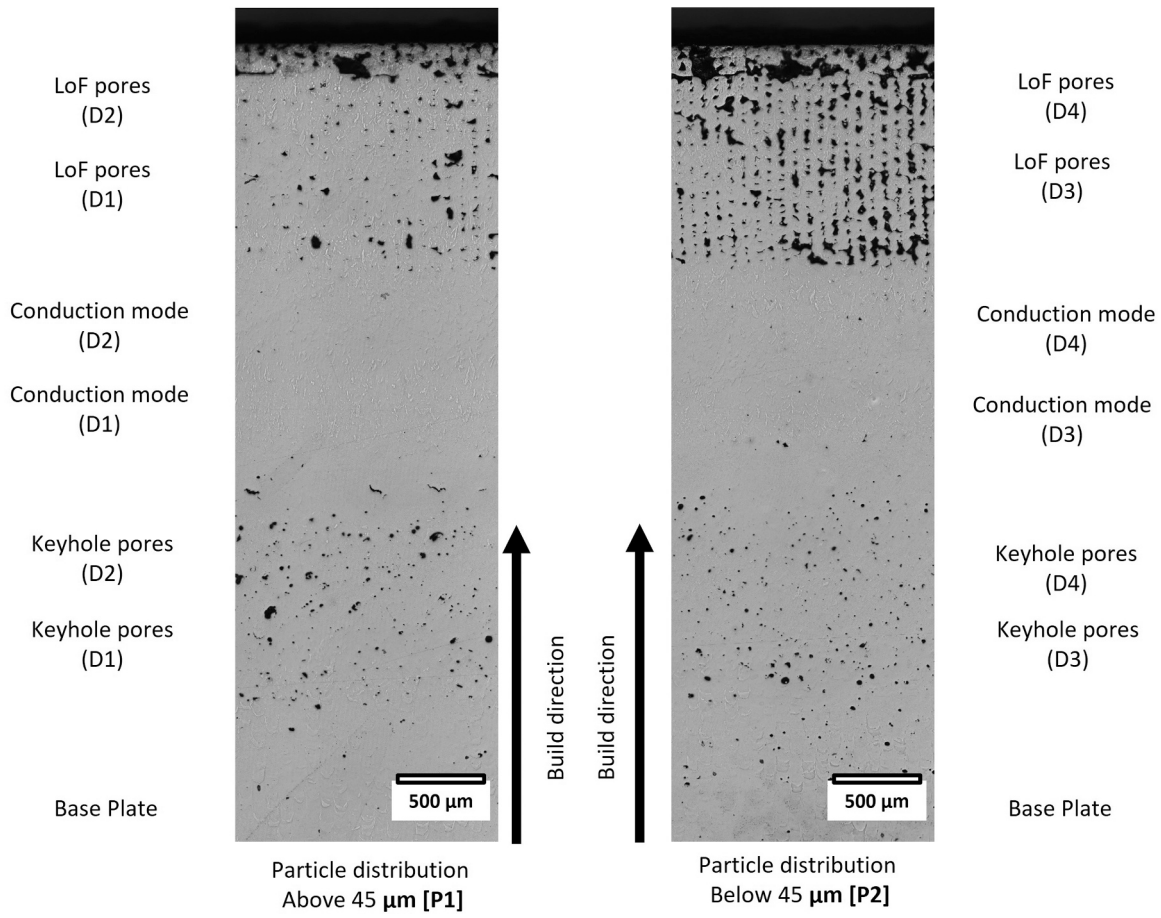


Fig. 5. Optical micrograph for each regime across three 316 L powder distributions *P1* and *P2*.

Table 3

The total number of 12.5 ms (5000 data points) AE windows that were extracted during the fabrication of the two cubes from particle distributions *P1* and *P2*.

| Particle distribution | Dataset name | Dataset size [windows] |
|--------------------------------------|--------------|------------------------|
| Above 45 μm [<i>P1</i>] | <i>D1</i> | 7500 [2500 / regime] |
| | <i>D2</i> | 7500 [2500 / regime] |
| Below 45 μm [<i>P2</i>] | <i>D3</i> | 7500 [2500 / regime] |
| | <i>D4</i> | 7500 [2500 / regime] |

2.5. Methodology

In this study, we developed two strategies to compute crucial frequency range importance for classification in LPBF regimes. These strategies serve distinct purposes and involve varied preprocessing levels, leading to different input configurations. The first strategy employs a 1D CNN to compute saliency over Intrinsic Mode Functions (IMFs) derived using EMD. This approach requires minimal preprocessing, and the CNN computes feature importance via saliency maps without additional steps. The input for this strategy is set at 7, corresponding to the 7 IMFs obtained through EMD, each carrying specific frequency information. The CNN's inherent capabilities facilitate this process seamlessly. In contrast, the second strategy involves a more complex process with additional preprocessing steps. This method entails feature computation, followed by using classifiers like XGBoost and SVM to evaluate classification accuracy. Subsequently, the feature importance and SHAP method are applied to the trained model to discern the importance score. The frequency information acquired from manual feature extraction is categorized into 15 bins. The feature computation was done with the periodogram method to compute

energies for fifteen frequency bands from 0 to 150 kHz across all dataset windows. This analysis also will provide insight into the AE waveform signal in the frequency domain.

These two strategies are distinct and serve different analytical purposes. While the first strategy leverages the inherent capabilities of a 1D CNN to compute saliency over IMFs, the second strategy involves a multi-step process incorporating classifiers with feature importance scores and SHAP analysis to assess feature importance. Given the fundamentally different nature of these strategies, a direct comparison between them may not be an ideal approach. Each strategy was designed to provide insights into sensor frequency dependence for decision-making from a unique perspective. Both strategies were validated through comprehensive experimentation and analysis on four different AE datasets.

3. Results and discussion

3.1. AE signal analysis

The frequency domain analysis was performed on the windows corresponding to each regime across all datasets (*D1-D4*) to confirm if changes in the offset in laser power parameters and distribution of powder particles have influenced the distribution of the acoustic signature from the process zone. The periodogram (Elliott, 2013) method was used to compute the energies for the fifteen frequency bands (0–10 kHz, 10–20 kHz, 20–30 kHz, 30–40 kHz, 40–50 kHz, 50–60 kHz, 60–70 kHz, 70–80 kHz, 80–90 kHz, 90–100 kHz, 100–110 kHz, 110–120 kHz, 120–130 kHz, 130–140 kHz, and 140–150 kHz) for all windows in the dataset to analyze the AE waveform signal in the frequency domain.

The results of the analysis of the cumulative energy values for the four datasets with three LPBF regimes across the fifteen frequency bands are presented in Fig. 6(a-d). It can be observed that the majority of energy components for all the powder distributions and laser parameters for the LPBF regimes are concentrated in the frequency range below 100 kHz for all four datasets. The peak energy of the AE waves for the *keyhole* regime was between 0 and 40 kHz. For the *LoF* regime, the dominant frequencies were between 10 and 90 kHz, while for the conduction regime, the dominant frequencies were between 10 and 90 kHz. The overall comparison of the cumulative energy distribution across the fifteen frequency bands confirms that deviations in the AE waves' energy content were due to the different dynamics of the process zone perturbations in the three regimes caused as a result of the laser power parameter and the powder particle distribution. Therefore, the correlation between specific AE information on LPBF regimes may be possible to utilized as a tool for monitoring the process quality. It should also be noted that further investigations are needed to understand the similarities in trends of AE signatures as a result of varying other process parameters. Addressing potential noise sources is crucial for accurate AE signal analysis. Noise can stem from various factors within the process chamber. Components moving, particularly the recoater mechanism, can contribute to noise, as can the laminar flow in the chamber. The microphone's directional sensitivity is key to managing and reducing this noise. This sensitivity allows the microphone to capture acoustic emissions from the process zone selectively. The microphone distinguishes real emissions from noise by recording AE data triggered only during laser interaction. This differentiation ensures precise and dependable AE signal analysis.

3.2. Empirical mode decomposition

Empirical Mode Decomposition (EMD) is a powerful signal processing technique that can decompose non-stationary signals into a simpler finite number of components that can be analyzed and used for various applications (Lei et al., 2013). The EMD performs signal decomposition in a time-series context, producing a series of constituent signals that comprise the original signal after processing. The linear combination of empirical modes can be used to reconstruct the original signal, $x(t)$,

using the EMD algorithm as depicted in Eq. (1).

$$x(t) = \sum_{i=1}^n c_i(t) + r_n(t) \quad (1)$$

where $c_i(t)$ is i -th empirical mode and $r_n(t)$ is the final residue after the extraction of n empirical modes. The resulting output of EMD remains in the time domain and does not assume the periodicity of the signal (Rilling et al., 2003). Instead, it uses Intrinsic Mode Functions (IMFs) that are more complex than simple sine waves. The term "empirical" in EMD reflects its approach of making no assumptions about the data. The EMD method does not have a specific mathematical formula, as it is a data-driven technique that uses four steps to decompose a signal into IMFs (Flandrin et al., 2004b). The first step involves identifying the signal's extrema (local maxima and minima). The second step connects the maxima and minima using cubic spline interpolation to form the upper $E_u(t)$ and lower $E_l(t)$ envelopes of the signal, respectively. A "mean envelope" ($m(t) = 0.5(E_u(t) + E_l(t))$) is computed as an average of the upper and lower envelopes in the third step. Finally, the difference between the original signal and the computed mean envelope is calculated, which is considered the first IMF. The process is repeated on the residual signal (original signal - first IMF), and subsequent IMFs are extracted from the residuals until the residuals become a constant or a monotonic function. Each IMF represents a simpler original signal component with its own local frequency, amplitude, and phase information. The final residual signal represents the trend component of the original signal. The IMF components can be further analyzed and used for various signal-processing tasks such as filtering (Wu and Huang, 2010), denoising (Flandrin et al., 2004a), feature extraction (Ali et al., 2015) and signal reconstruction (Flandrin et al., 2004b). EMD faces a significant issue known as mode mixing, which results in the loss of physical interpretation for individual IMFs. This phenomenon occurs when a single IMF comprises multiple intrinsic oscillation modes or when a single intrinsic oscillation mode is present in multiple adjacent IMFs (Tang et al., 2012).

In this work, the IMFs extracted from using EMD on the waveform AE signals $x(t)$ corresponding to the three regimes are analyzed to understand the underlying dynamics of the signal. The decision to employ EMD was grounded in retaining the signals' temporal nature and

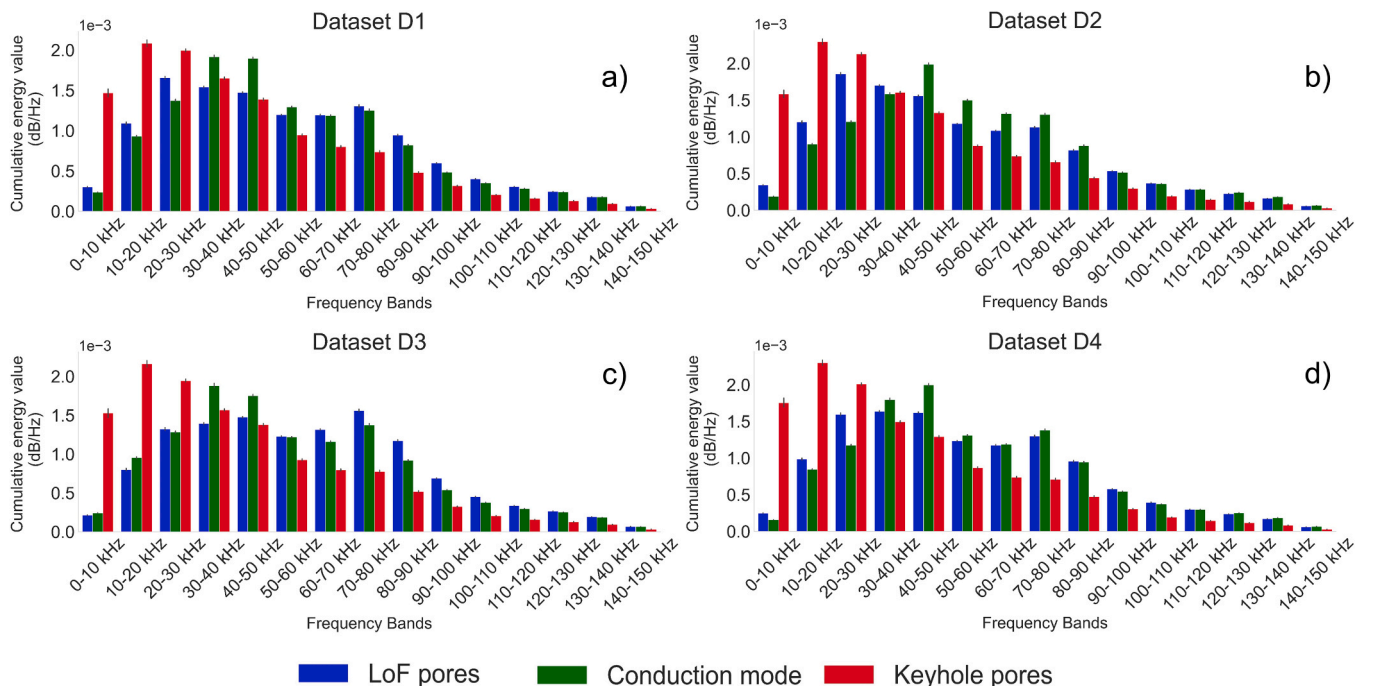


Fig. 6. Comparison of cumulative energy content between fifteen frequency bands for three regimes across four AE datasets.

avoiding transformations or statistical reduction techniques like feature extraction, spectrograms and wavelets. The EMD was chosen to disintegrate the time series signals into distinct frequency bins while preserving their temporal characteristics, aligning with the study's objectives. The visualization of the intrinsic modes computed using EMD on raw AE waveform of 12 ms corresponding to *LoF pore*, *conduction mode* and *keyhole pores* are shown in Fig. 7, Fig. 8 and Fig. 9. The choice of IMFs for seven levels was based on their characterization of them in the frequency domain. Interpolation of the computed IMF in the frequency domain, as shown in Fig. 7(b), Fig. 8(b) and Fig. 9(b), reveals that individual levels of IMFs carried information corresponding to different frequency contents. It could also be revealed that the frequency content across IMFs is arranged from higher to lower, as expected. The range of frequencies across the 7-IMFs is listed in Table 4. It can be easily

found from Fig. 7(a), Fig. 8(a) and Fig. 9(a) that the phenomenon of mode mixing exists in intrinsic mode oscillations.

A significant statistical dissimilarity was discovered when the envelope spectra of all seven IMF components associated with the three LPBF regimes were visualized and compared. This observation implies that the presence of statistical dissimilarity in the IMFs' envelopes can be utilized to train a classifier that can differentiate between the three LPBF regimes. This study's use of a 1D CNN is rooted in its seamless compatibility with raw data and temporal waveforms, eliminating the need for preprocessing steps. This choice aligns perfectly with the nature of the analyzed AE signals. The CNNs are well-suited for handling such data and facilitating saliency computation. This pivotal feature of saliency computation aids in mapping decision-making processes based on input space, crucially ranking the importance of information derived

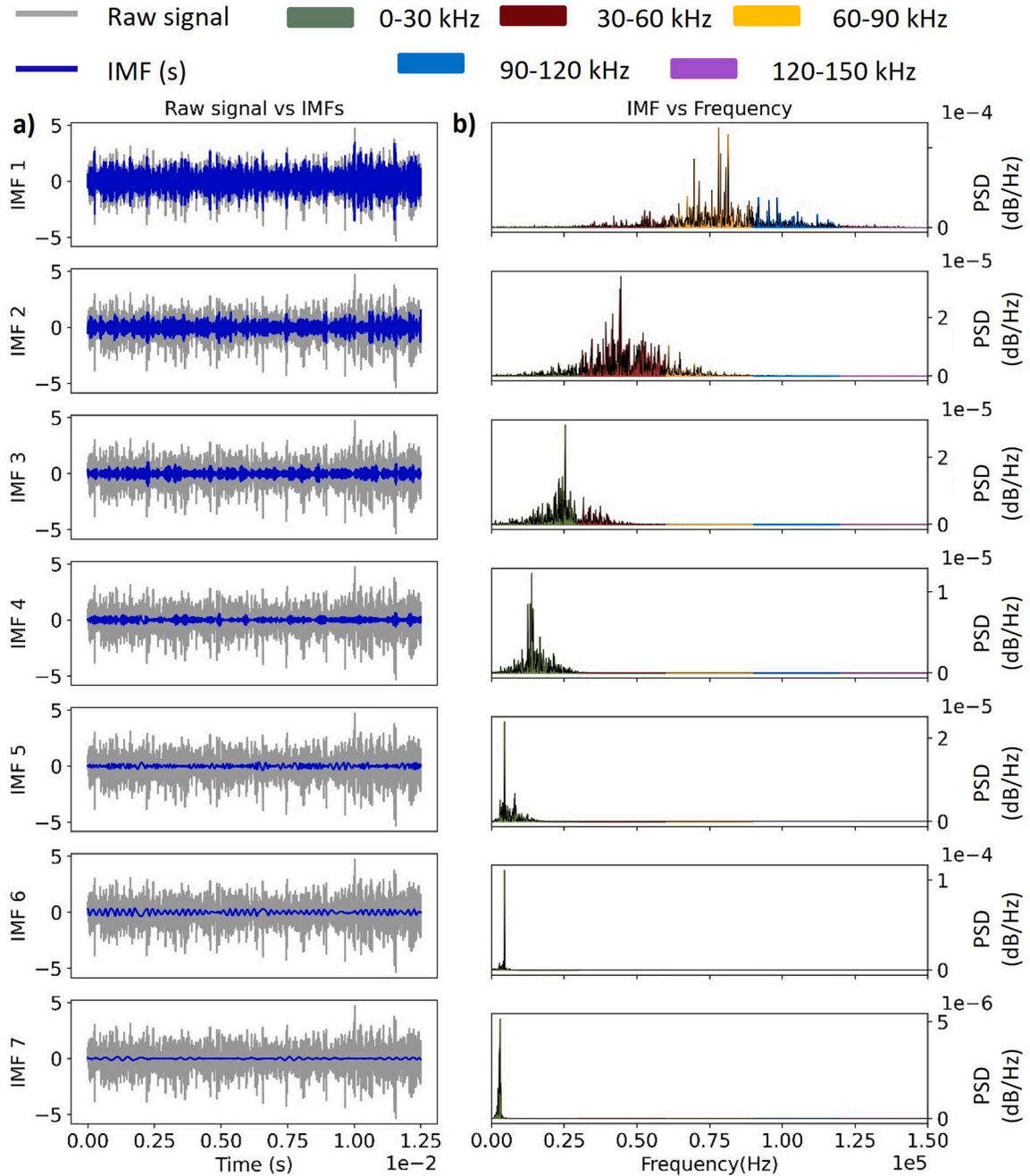


Fig. 7. (a) Intrinsic modes computed using EMD on raw AE waveform of 12 ms (Dataset D1) corresponding to *LoF pores*. (b) Frequency characterization of the individual extracted IMFs computed using EMD.

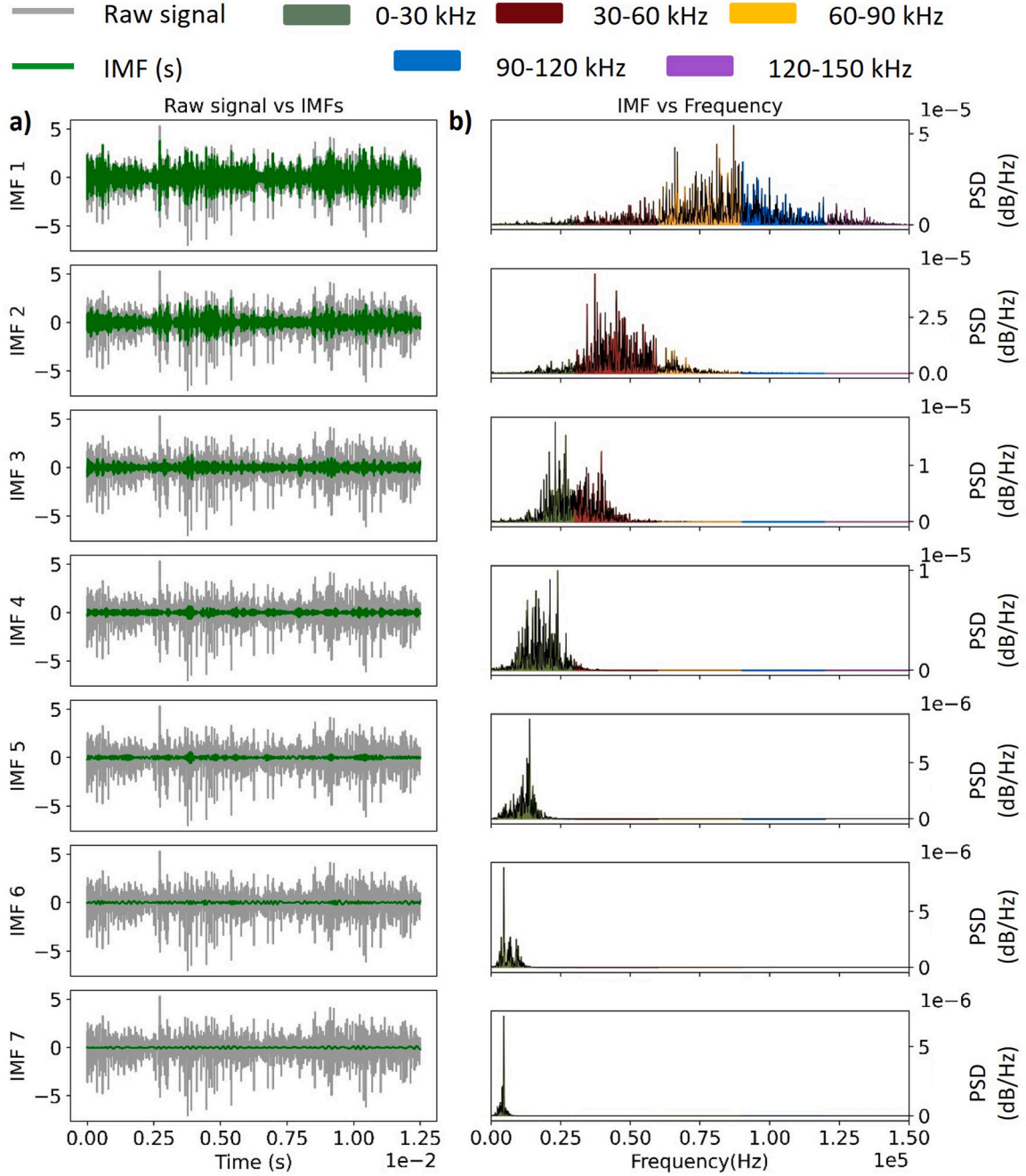


Fig. 8. (a) Intrinsic modes computed using EMD on raw AE waveform of 12 ms (Dataset D1) corresponding to *conduction mode*. (b) Frequency characterization of the individual extracted IMFs computed using EMD.

from EMD-computed intrinsic modes. The choice of the 1D CNN variant stemmed from inherent benefits in training parameters and pre-processing and the minimum computation resources required, unlike a 2-Dimensional CNN, which requires conversion to a spectrogram or wavelet representation with more computation requirements. The monitoring approach proposed in this study involves creating a 1D CNN classifier trained on the extracted IMFs for seven levels on AE waveforms with a time window of 12.5 ms to distinguish between different LPBF regimes. Additionally, it was discovered that the EMD functions as a dyadic filter bank that resembles the ones used in wavelet decompositions to control information across each IMF. This characteristic can be exploited by using saliency techniques (Parvatharaju et al., 2021) to identify which IMF modes correspond to more weightage for decision-making during inference.

3.2.1. 1D-CNN – Classifier

The 1D-CNN model proposed in this work to train the four datasets (D1-D4) consists of five convolutional layers, one Fully Connected layer (FC –1), and a classifier layer, as illustrated in Fig. 10. The input tensor of size $1 \times 7 \times 5000$ is passed through the first layer of the CNN model during training. The second dimension of the input tensor represents the seven IMFs obtained using the EMD technique. All five convolutional layers of the CNN architecture have a kernel size of 16. The first convolutional layer generates an output size of four, which is then doubled in size in each subsequent layer until the fifth layer. The output size of the fifth convolutional layer is 64 with a single dimension, which was achieved by applying an adaptive pooling technique on a single dimension. The output of these five convolutional layers is then flattened and passed to a fully connected layer and a classification layer for

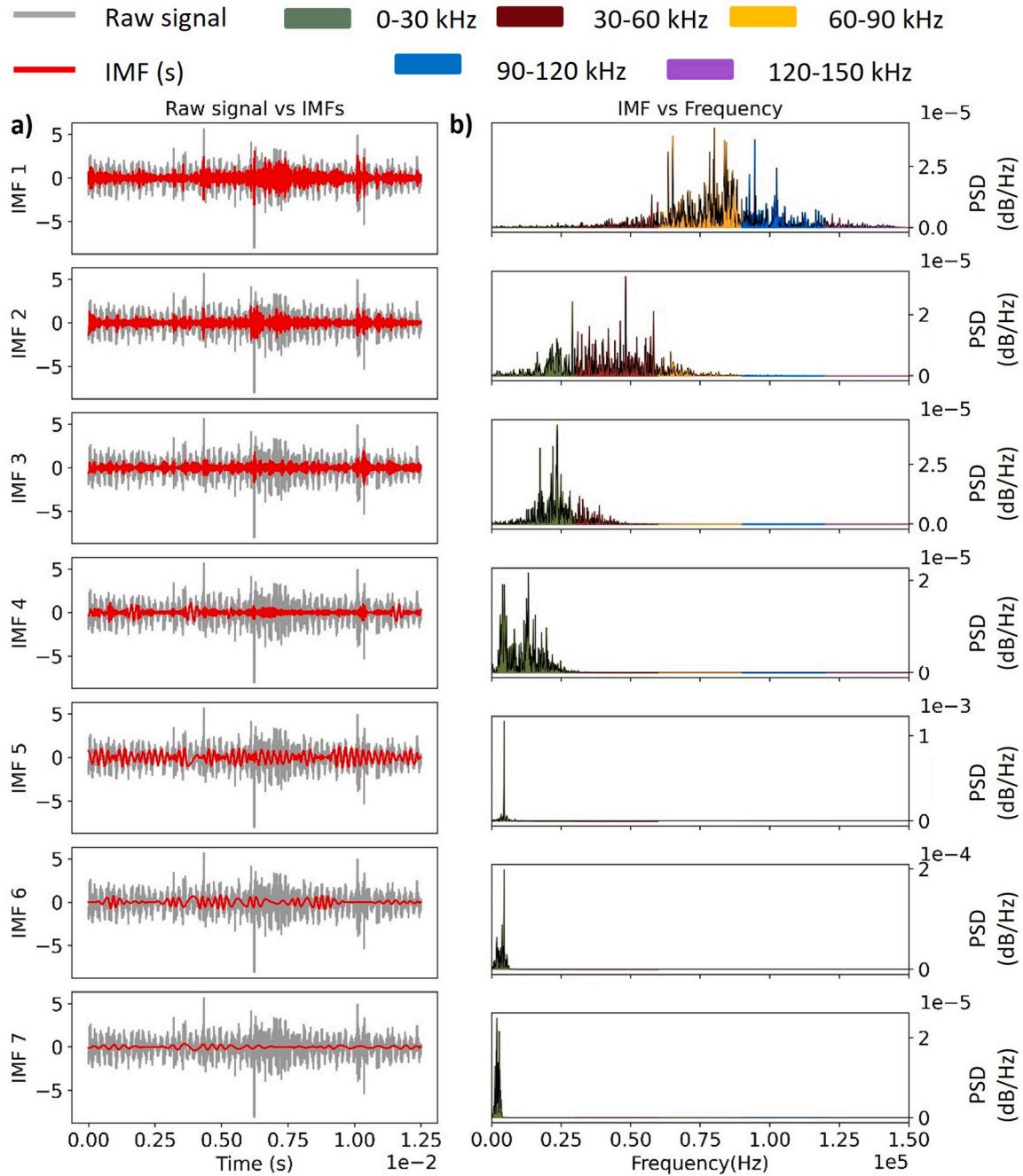


Fig. 9. (a) Intrinsic modes computed using EMD on raw AE waveform of 12 ms (Dataset D1) corresponding to *keyhole pores*. (b) Frequency characterization of the individual extracted IMFs computed using EMD.

Table 4

Frequency contents across individual extracted IMFs computed using EMD.

| IMF's | Frequency ranges |
|-----------|------------------|
| Level - 1 | 60–100 kHz |
| Level - 2 | 30–70 kHz |
| Level - 3 | 25–40 kHz |
| Level - 4 | 15–25 kHz |
| Level - 5 | 10–20 kHz |
| Level - 6 | 5–15 kHz |
| Level - 7 | 0 kHz–10k Hz |

further processing. The labelled signals corresponding to the four AE datasets computed using EMD are used for training four individual networks, namely *CNN-1*, *CNN-2*, *CNN-3* and *CNN-4*, for classifying them into *LoF*, *condition mode*, and *keyhole*. The cross-entropy loss function is used for this classification problem.

The proposed 1D CNN model has approximately 47 thousand parameters and was developed using the PyTorch framework. Batch normalization is performed across each layer before applying the Rectified Linear Unit (ReLU) activation function. Additionally, a dropout of 5% is applied across the layer to reduce overfitting. The use of dropout is a regularisation technique that helps to prevent overfitting by randomly dropping out some neurons during training, which forces the network to learn more robustly. The training parameters used for the training of the four CNN models are listed in Table 5. These parameters

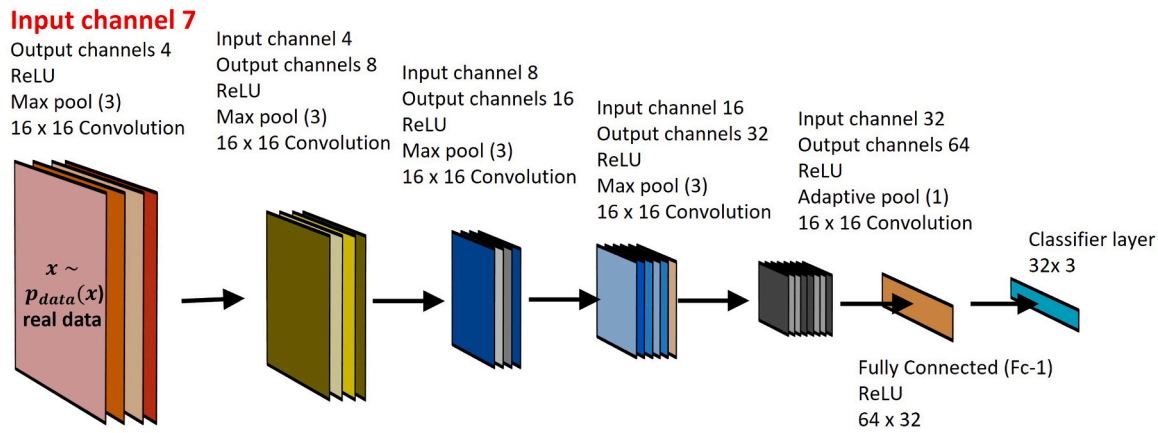


Fig. 10. Illustration of the proposed CNN network.

Table 5

Training parameters for training CNN-1, CNN-2, CNN-3 and CNN-4.

| Training parameters | CNN-1, CNN-2, CNN-3 and CNN-4 |
|---------------------|-------------------------------|
| Objective | Supervised classification |
| Solver type | 'adam' |
| Rate of learning | 0.01 |
| Epochs | 100 |
| Size of the batch | 256 |
| Dropout | 5% |
| Loss function | Cross-entropy loss |
| Shuffle | Every-epoch |
| Scheduler used | Cosine annealing |
| Training dataset | 70% |
| Testing dataset | 30% |
| Trainable weights | 46,395 parameters |

were drawn from the authors' prior works using the same architecture (Pandiyan et al., 2022b) and combined with empirical optimization through trial and error.

The extracted IMFs for seven levels on AE waveforms with a time window of 12.5 ms corresponding to three regimes were used to train the model during the processing of datasets (D1-D4). The AE dataset collected with known labels was randomly divided into 70% for training and 30% for testing. During network training, the cross-entropy loss was utilized to punish the network for misclassifications. In addition, the magnitude of the cross-entropy loss was used to update the weights of CNNs through back-propagation. CNNs were trained using a batch size of 256 and a learning rate of 0.01 for 100 epochs. Nvidia Titan RTX GPU was used to expedite the training process. A cosine annealing-based learning rate scheduler was employed to find the optimal learning rate across each epoch. The training loss values for all four CNN models decreased over the course of 100 training epochs, indicating that they have successfully learned how to map the AE signals and classify the three LPBF regimes. Table 6 presents the confusion matrix that provides a clear and concise summary of the model's predictive accuracy and errors. The overall prediction accuracy of the four CNN models ranged between 95.3% and 96.9%. However, the global accuracy on different datasets suggests that the proposed CNN architecture could be scaled to similar classification tasks.

3.2.2. CNN- Saliency maps

Saliency maps are a visualization technique used in CNNs to highlight the most relevant parts of the input data for making a prediction. These maps are created by calculating the Gradient of the output class score with respect to the input data, which shows how sensitive the network is to changes in the input data. For time series data, saliency maps indicate which regions of the waveform the network is focusing on when making its classification decision (Assaf et al., 2019). The

Table 6

Confusion matrix from the CNNs on four datasets (D1, D2, D3, and D4).

| True class | LoF | Conduction mode | Keyhole |
|-----------------|------------------------------|------------------------------|------------------------------|
| Predicted class | | | |
| LoF | 97.4 98.0 96.8 94.7 | 2.6 1.6 3.2 5.3 | 0.0 0.4 0.0 1.0 |
| Conduction mode | 5.2 4.9 2.2 2.4 | 93.8 94.0 96.3 96.1 | 1.0 1.1 1.5 1.5 |
| Keyhole | 2.2 1.3 1.2 2.4 | 0.7 1.0 1.2 2.2 | 97.1 97.7 97.6 95.3 |

The four datasets are represented in a confusion matrix that displays the classification accuracies, with the classification outcomes arranged in descending order within each cell: D1, D2, D3, and D4. All values are in %.

magnitude of the gradient at each time series datapoint indicates the importance of that datapoint for the final prediction (Pandiyan et al., 2022b). The resulting saliency map has values between 0 and 1, where higher values indicate more salient data points. The saliency map's size corresponds to the input signal's length.

The saliency analysis depicted in Fig. 11 (a-d) provides insight into the relative importance of the median saliency, which was computed per IMF, on the test datasets for each of the four models (CNN-1, CNN-2, CNN-3 and CNN-4). The analysis specifically focuses on predictions that were correctly classified. By examining the saliency scores of each IMF, the study demonstrates the relative significance of different frequency components present in the input data. The findings suggest that certain IMFs (from 3 to 7), particularly those with lower frequency components below 40 kHz, contribute more significantly to the decision-making process. The saliency score computed for the four models was normalized to 1 across all seven levels of IMFs as depicted in Fig. 11. The analysis revealed that IMFs ranging from level 3 to level 6 played a more significant role in the decision-making process, contributing over 70% to the final decision for all four cases. Moreover, these IMFs contained frequency components between 0 and 40 kHz, which suggests the importance of the frequency window of the sensor in these ranges for accurate monitoring of LPBF regimes during the processing of 316 L. These results suggest that identifying the relative significance of different frequency components can enhance the accuracy of predictions and decision-making in LPBF processes, leading to more efficient and effective LPBF-based manufacturing.

The study found that the input tensors' dimensions, specifically IMFs 3–7, containing frequency ranges below 40 kHz, played a dominant role

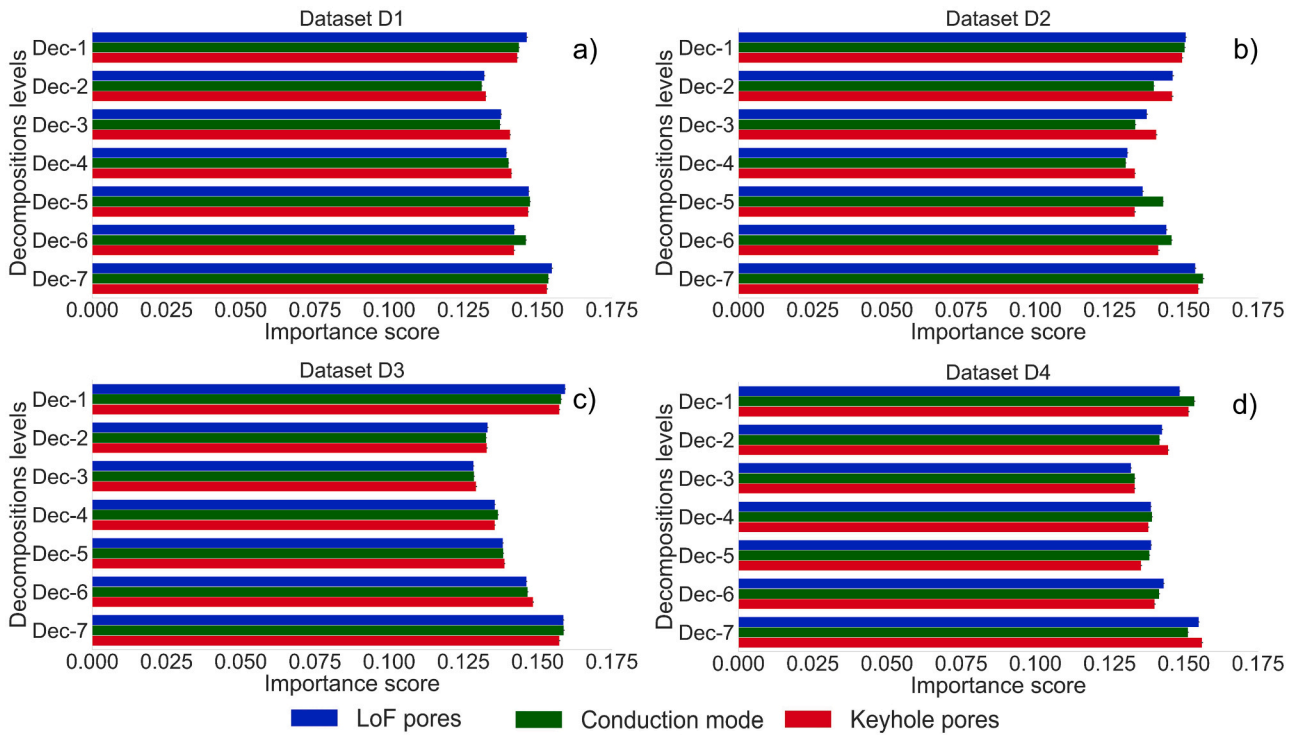


Fig. 11. Saliency analysis per decomposition level for four datasets (D1, D2, D3, and D4) using four CNN models (CNN-1, CNN-2, CNN-3 and CNN-4).

in the prediction process. However, it is essential to note that the number of IMFs containing overlapping information below 40 kHz was relatively high compared to the IMFs carrying information above 40 kHz. Therefore, it is also crucial to validate the sensor frequency dependence for decision-making using other classical classification techniques that do not have such biasing and overlapping but look at discrete statistical information. To achieve this goal, the study used energies for the fifteen frequency bands computed in 3.1 as features to train classifiers such as XGBoost and SVM as shown in Fig. 12. Eventually, the feature metrics' importance was evaluated to check if any coherence was found with saliency results. By cross-validating these

results, the study can better understand the importance of sensor frequency ranges in LPBF monitoring and further improve the accuracy of predictions and decision-making.

3.3. XGBoost and Feature Importance

Ensemble learning is often employed to mitigate the issues of bias and variance commonly found in individual models (Zhou and Zhou, 2021). This approach involves creating a model that leverages the predictions of multiple individual models. By doing so, the ensemble model becomes more adaptable (less biased) and less susceptible to changes in

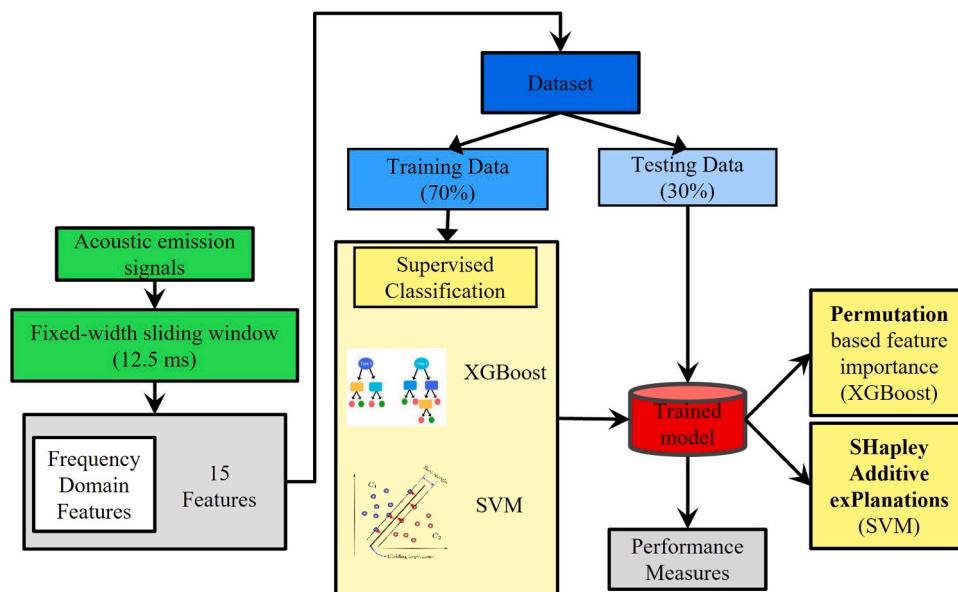


Fig. 12. Schematic flow for classifying LPBF regimes in 316 L using two ML models with 15 frequency features for computing feature importance on four datasets (D1, D2, D3, and D4).

the input data (less variance). XGBoost, which stands for eXtreme Gradient Boosting, is an example of an ensemble model that uses boosting and decision trees as multiple individual models. It is a versatile tree-boosting system that can be used for classification and regression tasks in machine learning and is known for its scalability (Chen et al., 2015). XGBoost involves creating a prediction model comprising an ensemble of weaker prediction models, such as decision trees. The model is built incrementally, and its generalization is achieved by optimizing an arbitrary differentiable loss function. Essentially, XGBoost helps reduce overfitting, improving its overall performance. XGBoost has several notable advantages over other algorithms, including its exceptional speed relative to algorithms like AdaBoost and the effectiveness of its regularisation parameter in reducing variance. In addition to this parameter, XGBoost employs a learning rate (shrinkage) and subsampling of features, similar to random forests, further improving its generalizability. However, compared to AdaBoost and random forests, XGBoost is more challenging to comprehend, visualize, and fine-tune. In addition, it has a multitude of hyperparameters that can be adjusted to enhance its performance. The energies for the fifteen frequency bands computed using the periodogram method, as discussed in Section 3.1, form a dataset that the classifier will learn. The implementation was carried out using the Python scikit-learn libraries (Pedregosa et al., 2011). The hyperparameters for training the XGBoost Classifier are trained using the settings listed in Table 7. Synonymous with the training of four CNN models on four datasets (D1-D4), the energies calculated from the fifteen frequency bands from each of the four datasets were used to create feature spaces for training four XGboost classifiers. These classifiers were named XG-1, XG-2, XG-3, and XG-4, and for training them, the respective datasets computed with known ground truth were randomly divided into 70% for training and 30% for testing.

The average performance of the four XG boost models was evaluated based on stratified-fold cross-validation. Table 8 presents the confusion matrix that provides a clear and concise summary of the predictive accuracy and errors of the model. The overall prediction accuracy of the XGBoost model on the six datasets ranged between 90% and 94.3%. Overall, the results suggest that XGBoost-based classifiers are a promising approach for LPBF monitoring. Current work demonstrates that the appropriate choice of the sensor with a wide range can significantly impact the classification of the LPBF regime with minimal features, and this finding is a departure from what has been reported in the literature.

Using a gradient-boosted model facilitates the retrieval of the importance score for each feature after the boosted trees have been built. The XGBoost permutation-based feature importance method, which involves randomly shuffling each feature and evaluating the resulting model performance change (Minhas and Singh, 2021), was used to retrieve the importance score for each feature after building the gradient-boosted model. Using this method, the study identified the features that significantly impacted the performance of the four models (XG-1, XG-2, XG-3, and XG-4) trained on the four datasets. Fig. 13 (a-d) shows the corresponding plots with the most informative content for the classification performance for the four XGboost classifiers. The significant features that contributed more to the four models' performance

Table 7

XGBoost classifier training parameters.

| Training parameters | XG Boost (XG-1, XG-2, XG-3, and XG-4) |
|---------------------|---------------------------------------|
| Rate of learning | 0.3 |
| Tree method | auto |
| Depth | 6 |
| Sampling method | uniform |
| gamma | 0.1 |
| subsample | 1 |
| colsample_bytree | 1 |
| Objective | classification |
| Validation method | Stratifiedfold cross-validation |

Table 8

Confusion matrix from the XGBoost on four datasets (D1, D2, D3, and D4).

| True class Predicted class | LoF | Conduction mode | Keyhole |
|-------------------------------|-------------------------------------|------------------------------|------------------------------|
| LoF | 91.0 96.0 88.0 95.0 | 8.0 3.0 12.0 4.0 | 1.0 1.0 0.0 1.0 |
| Conduction mode | 10.0 7.0 9.0 10.0 | 89.0 91.0 87.0 88.0 | 1.0 2.0 4.0 2.0 |
| Keyhole | 1.0 2.0 2.0 3.0 | 4.0 2.0 3.0 3.0 | 95.0 96.0 95.0 94.0 |

The four datasets are represented in a confusion matrix that displays the classification accuracies, with the classification outcomes arranged in descending order within each cell: D1, D2, D3, and D4. All values are in %.

came from the frequency components in signals below 50 kHz. Energies for frequency bands below 50 kHz were deemed the most critical in decision-making, ranking higher with a high feature importance score. These findings are consistent with the saliency maps computed on CNNs, as discussed in Section 3.2.1. Based on the results of feature importance, the study emphasizes the importance of sensor frequency response at lower frequencies in monitoring LPBF regimes when processing 316 L.

One of the limitations of using a gradient-boosted model in interpreting the overall feature importance score is that it does not give insight into which categorical dependent variable is being influenced. In other words, it is unclear which categorical variables drive the model's predictive power. To address this limitation, SHapley Additive exPlanations (SHAP) values, which provide more detailed and relevant information on the categorical dependent variable, are explored in the upcoming Section 3.4 on Support Vector Machine (SVM). SHAP values measure the contribution of each feature to the final prediction, taking into account the interactions between features and providing a more nuanced understanding of how the model makes its predictions.

3.4. SVM and Shapley Additive Explanations

Support Vector Machine is a popular supervised learning algorithm used for classification and regression analysis. The SVM aims to find the best hyperplane that separates the different classes in a dataset (Hearst et al., 1998). The hyperplane is chosen to maximize the margin between the closest points of different classes, also known as support vectors (Cervantes et al., 2020). It can handle non-linearly separable data by transforming the original feature space into a higher dimensional space where the classes are separable (Pandiyan et al., 2018). The SVM has several advantages over other classification algorithms, including its ability to handle high-dimensional data and its effectiveness in handling small to medium-sized datasets. However, due to its computational complexity, SVM may not perform well on very large datasets. The optimization problem of SVM involves finding the parameters of the hyperplane that minimize the classification error and maximize the margin. This is done by solving a quadratic programming problem where the objective function is the sum of the squares of the weights of the hyperplane subject to the constraint that the data is classified correctly. If the data is not linearly separable, SVM uses a kernel function to map the original feature space into a higher dimensional space where the classes are separable. This allows SVM to handle non-linear decision boundaries. Standard kernel functions used in SVM include linear, polynomial, Radial Basis Function (RBF), and sigmoid. Similar to the training of the four CNN models and four XGBoost classifiers, the energies computed from the fifteen frequency bands from each of the four datasets (D1-D4) were utilized to create feature spaces for training four SVM classifiers. These classifiers were named SVM-1, SVM-2, SVM-3,

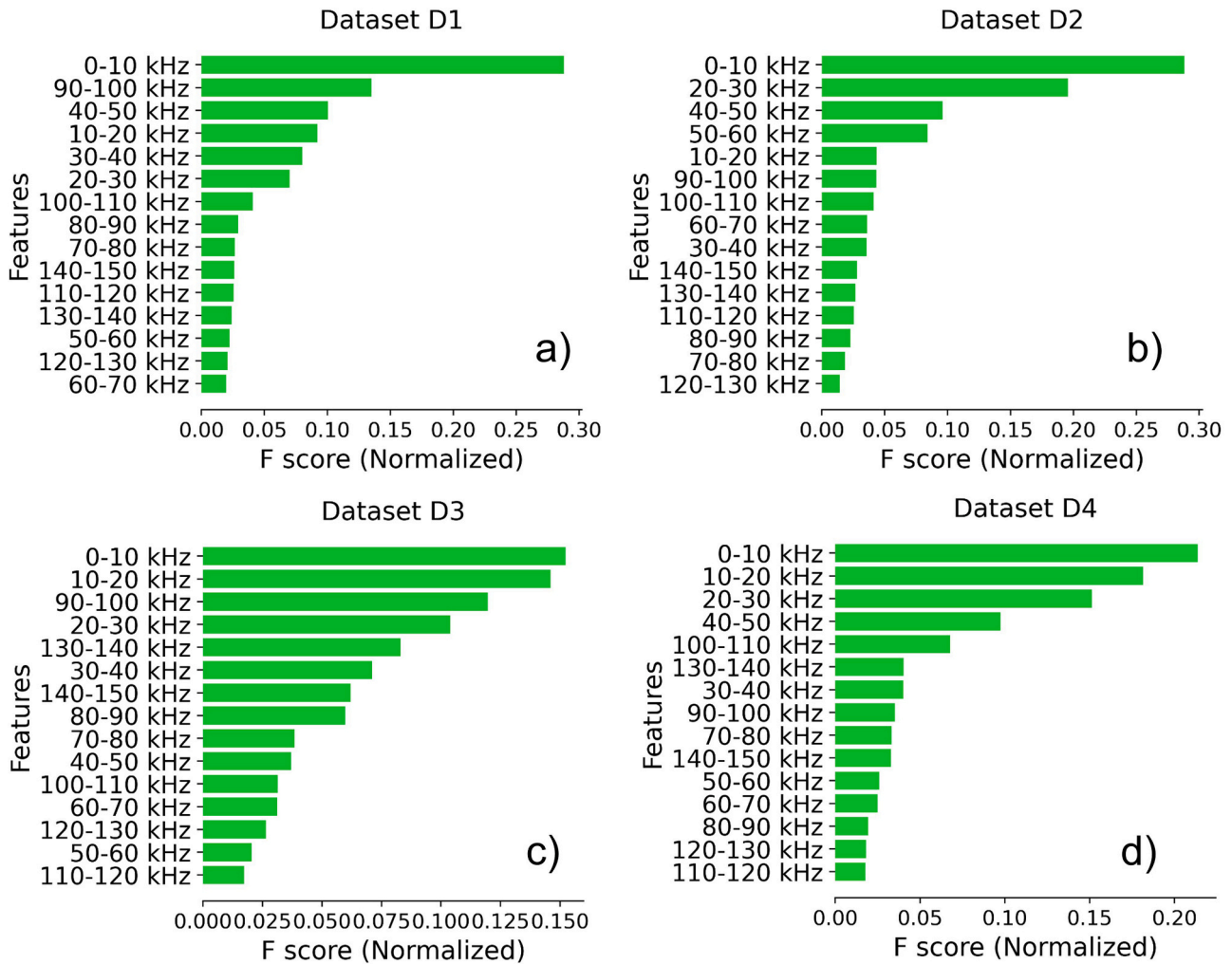


Fig. 13. Permutation-based feature importance for four datasets (D1, D2, D3, and D4) with four models (XG-1, XG-2, XG-3, and XG-4).

and SVM-4. For training these classifiers, each dataset was randomly divided into 70% for training and 30% for testing, with known ground truth. The implementation was carried out using the Python libraries scikit-learn (Pedregosa et al., 2011). The hyperparameters used for training the SVM classifier are listed in Table 9.

Table 10 presents a confusion matrix summarising the model's accuracy and errors concisely and easy to understand. The SVM models (SVM-1, SVM-2, SVM-3, and SVM-4) that were trained on the four datasets individually exhibited an overall prediction accuracy ranging from 85.0% to 89.6%. These results indicate that SVM-based classifiers could be a promising method for monitoring LPBF using a feature space with only 15 dimensions. The current study demonstrates that the appropriate choice of a sensor with a wide range can significantly impact

Table 9

Training parameters on SVM models trained on four datasets (D1, D2, D3, and D4).

| Training parameters | SVM-1, SVM-2, SVM-3, and SVM-4 |
|---------------------|---------------------------------|
| Analysis | Supervised classification |
| Validation method | Stratifiedfold cross-validation |
| Kernel | Radial Basis Function |
| Kernel scale | Automatic |
| Features | 15 features |
| Classifiers | 3 (LPBF regimes) |
| Multiclass method | One-vs-One |
| Training dataset | 70% |
| Testing dataset | 30% |

Table 10

Confusion matrix from the SVM on four datasets (D1, D2, D3, and D4).

| True class Predicted class | LoF | Conduction mode | Keyhole |
|-------------------------------|------------------------------|------------------------------|------------------------------|
| LoF | 90.0 95.0 86.0 90.0 | 9.0 4.0 12.0 8.0 | 1.0 1.0 2.0 2.0 |
| Conduction mode | 15.0 12.0 14.0 14.0 | 83.0 88.0 81.0 86.0 | 2.0 0.0 5.0 0.0 |
| Keyhole | 9.0 10.0 4.0 10.0 | 8.0 4.0 8.0 5.0 | 83.0 86.0 88.0 85.0 |

The four datasets are represented in a confusion matrix that displays the classification accuracies, with the classification outcomes arranged in descending order within each cell: D1, D2, D3, and D4. All values are in %.

the classification of the LPBF regime with minimal features, which is a departure from what has previously been reported.

The SHAP is a popular approach for explaining the output of machine learning models. SHAP is based on the concept of Shapley values, which are used in game theory to determine the contribution of each player to a cooperative game (Nohara et al., 2019). In ML, SHAP values are used to explain each feature's contribution to a model's output for a specific

input. SHAP provides a unified framework for explaining the output of a wide range of models, including tree-based models, linear models, neural networks, and more. SHAP computes each feature's contribution to the model's output by assigning a score to each feature that reflects its impact on the model's prediction. SHAP values are computed using a variant of the LIME (Local Interpretable Model-Agnostic Explanations) approach, which generates local models to approximate the behaviour of the original model around a specific input. SHAP combines the local models to obtain a global explanation of the model's behaviour. SHAP has several advantages over other model interpretation methods. It provides a unified framework for interpreting a wide range of models and can handle both individual instances and entire datasets. SHAP also provides a measure of feature importance that takes into account the interaction between features, which is especially useful for non-linear models. By using SHAP, you can gain insights into how each feature contributes to the model's predictions and understand the importance of each feature in the context of the entire dataset. This can help you to

identify which features are most important in predicting house prices and make more informed decisions based on the model's output.

The results on the SHAPley values, which significantly impacted the performance of the four models (*SVM-1*, *SVM-2*, *SVM-3*, and *SVM-4*) trained on the four datasets, are illustrated in Fig. 14. The SHAPley values that provided the most informative content for better performance of the four models came from the frequency components in signals below 40 kHz. The magnitude of SHAPley values indicated that energies for the frequency bands below 40 kHz had the most influence on the decision-making process. Further looking for insights into which categorical dependent variable is being influenced as plotted in colour code (*red*, *blue* and *green*) in Fig. 14 (a-d), it is evident that all three regimes (categories) have an equal magnitude and are significantly important. Based on these SHAPley value results, the study emphasizes the importance of sensor frequency ranges (0–40 kHz) in monitoring LPBF regimes when processing 316 L. This finding is similar to the saliency maps computed on CNNs discussed in Section 3.2.1. and the

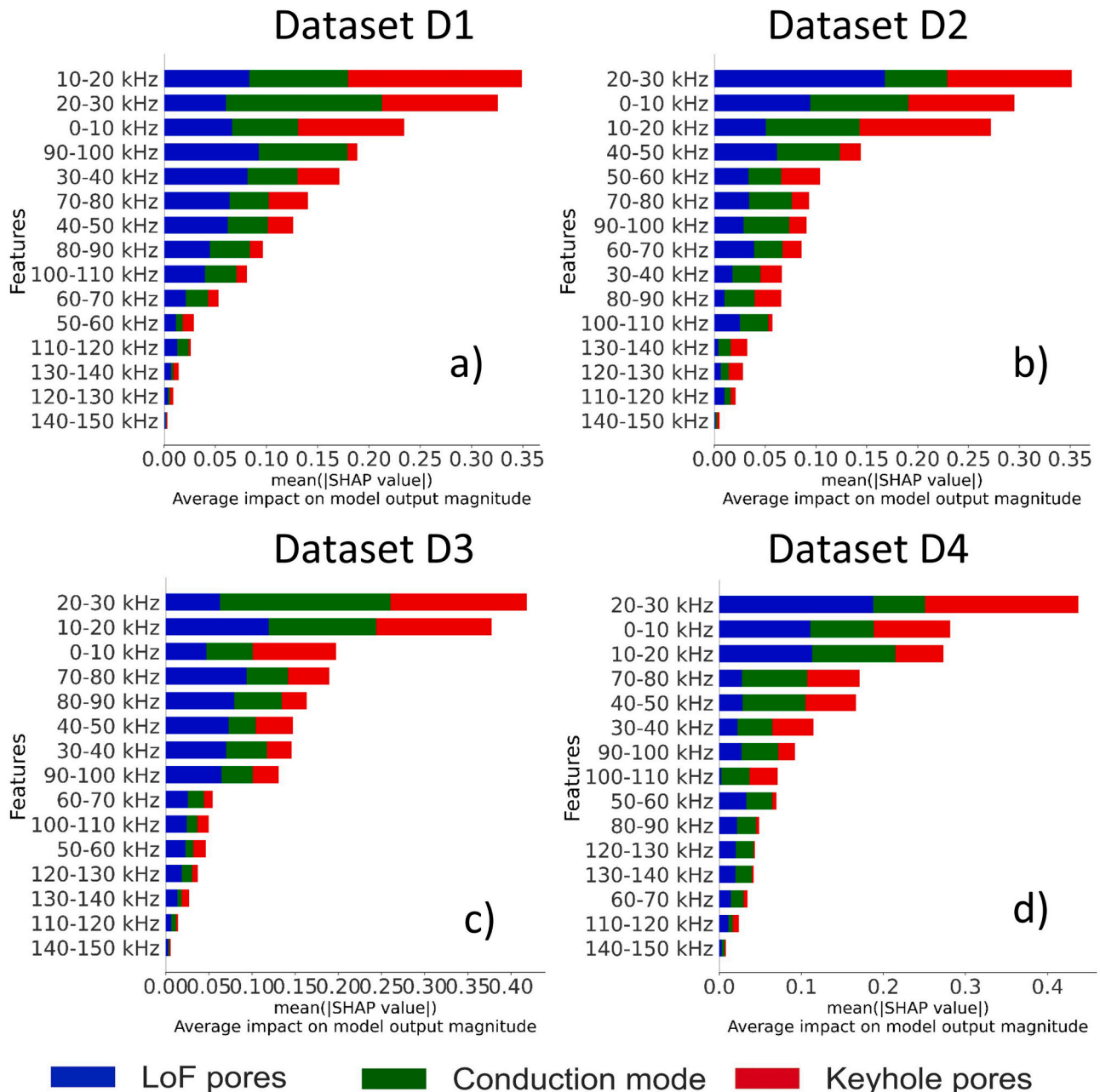


Fig. 14. SHAPley values on features in the four datasets (*D1*, *D2*, *D3*, and *D4*) computed over trained SVMs (*SVM-1*, *SVM-2*, *SVM-3*, and *SVM-4*).

permutation-based feature importance with XGBoost, as discussed in Section 3.3.

4. Discussion

The current study underscores the significance of airborne AE sensor selection based on its sensitivity to LPBF dynamics and its effect on the accuracy of LPBF regime classification, an aspect that previous studies did not explore or did not consider. The selection of an airborne AE sensor with poor sensitivity resulted in the utilization of a more significant number of features in the classification task, as reported by the author's previous work (Drissi-Daoudi et al., 2022). However, this work highlights the significance of selecting an AE sensor with a wide frequency response window, which is critical in achieving high accuracy with minimal features. These findings suggest that sensor selection should be a critical consideration in LPBF process monitoring, and further research may be necessary to identify the most optimized sensors for this task. The study's extensive exploration, involving two strategies on four datasets, contributes to the robustness and credibility of these findings.

Additionally, a framework for an airborne AE sensor selection strategy for monitoring LPBF during the processing of 316 L is developed. The study found that selecting a sensor from 0 to 40 kHz with good sensitivity response would suffice in real-time build quality monitoring of 316 L. The proposed strategy of computing saliency over the IMFs and estimating feature importance over handcrafted features have enhanced the knowledge of the correlation of LPBF dynamics with airborne AE signatures. Furthermore, the proposed framework is scalable and could be expanded to identify the significant frequencies for optimizing sensor selection that is good in sensing process zone perturbations of other materials during LPBF processing. Additionally, the proposed framework is not limited to a specific application and can be applied to other scenarios with similar sensing requirements. By identifying the significant frequencies most effective in detecting anomalies in the process zone, the framework can help researchers and engineers optimize their sensor selection and improve the accuracy and efficiency of their process sensing.

5. Conclusion

The paper analyses the AE signals captured during the LPBF process under three different regimes using two distinct distributions of 316 L stainless steel powders. The experiments were conducted on a commercial LPBF machine equipped with a custom-designed monitoring system for capturing and interpreting the AE signals. To understand the AE thoroughly, the study collected data for two different powder distributions of 316 L stainless steel, namely those with particle sizes greater than 45 μm and less than 45 μm , using two different parameter sets that encompassed a broad range of process conditions. In addition, the paper performed statistical quantification of the acoustic signals corresponding to three different regimes using frequency domain and Empirical Mode Decomposition (EMD) analysis. The resulting data were then visualized to help better understand the underlying physics of the AE on LPBF dynamics. The experimental results led to the following generalized conclusions:

- The energies of the AE waveform signal were visualized by dividing them into fifteen equally distributed bands from 0 Hz to 150 kHz. The results showed that the three LPBF dynamics being studied had distinct energy levels that were statistically significant across all the fifteen bands.
- Most of the energy components for the LPBF regimes were observed to be concentrated in the frequency range below 100 kHz. Compared to other regimes, the keyhole regime had a higher peak energy of the AE waves on frequency ranges between 0 and 10 kHz. The fifteen

bands' discrete energy levels could be leveraged as input to train an ML classifier for process monitoring.

- Moreover, EMD was employed to decompose the AE signals corresponding to different LPBF regimes into their constituent signals, which were subsequently compared. The characterization and visualization of the intrinsic mode envelopes in FFT for seven levels revealed the existence of mode mixing and a substantial level of statistical dissimilarity.
- The monitoring approach proposed in this study entails the creation of a 1D CNN classifier that can differentiate between various LPBF regimes based on the extracted IMFs for seven levels on AE waveforms. The time window for this approach was set to 12.5 ms. Upon computing saliency on the test data, it was found that the lower frequency components in the intrinsic modes, particularly those below 40Khz, contained the most informative content for decision-making.
- The computation of feature importance and Shapley scores on the XGBoost and SVM classifiers enabled the identification of the frequency ranges in the AE data that are critical in distinguishing between different LPBF regimes. These results were consistent with the findings of the saliency computation on the 1D CNN, indicating that the lower frequency ranges contain the most informative content.

Moving forward, an important avenue for future research involves expanding the scope of exploratory data analysis to encompass a broader spectrum of process parameters, as the current study was limited to only three process parameters. This would enable a comprehensive understanding of the intricate behaviour of AE signatures and their dynamic response to diverse parameters, further enhancing our insights into their impact and magnitude. The proposed framework has the potential to be expanded to identify frequencies associated with other types of events, such as delamination, crack propagation, and microstructure evolution, an ongoing research direction. Exploring frequencies associated with process zone perturbations in materials other than those currently being studied is also part of our future work. The data and code used for this work can be found in the following repositories (<https://c4science.ch/diffusion/12858/>).

CRediT authorship contribution statement

Vigneashwara Pandiyan: Conceptualization, Investigation, Formal analysis, Methodology, Software, Data curation, Writing- Original draft preparation. **Rafał Wróbel:** Investigation, Formal analysis, Data curation, Methodology Writing- Reviewing and Editing. **Christian Leinenbach:** Resources, Writing- Reviewing and Editing, Supervision, Project administration, Funding acquisition. **Sergey Shevchik:** Validation, Writing- Reviewing and Editing, Supervision.

Declaration of Competing Interest

The authors declare that they have no known competing financial interests or personal relationships that could have appeared to influence the work reported in this paper.

Data Availability

The data and code used for this work can be found in the following repositories (<https://c4science.ch/diffusion/12858/>).

Acknowledgement

V.P. would like to acknowledge the financial support of the project "CRSII5_193799 / 1" entitled "In situ monitoring in additive manufacturing of metals and alloys based on artificial intelligence" from the program of the Swiss National Science Foundation (SNSF).

References

- Ali, J.B., Fnaiech, N., Saidi, L., Chebel-Morello, B., Fnaiech, F., 2015. Application of empirical mode decomposition and artificial neural network for automatic bearing fault diagnosis based on vibration signals. *Appl. Acoust.* 89, 16–27.
- Assaf, R., Giorgi, I., Bagehorn, F., Schumann, A., 2019. Mtex-cnn: Multivariate time series explanations for predictions with convolutional neural networks, 2019 IEEE International Conference on Data Mining (ICDM). IEEE, pp. 952–957.
- Bartlett, J.L., Heim, F.M., Murty, Y.V., Li, X., 2018. In situ defect detection in selective laser melting via full-field infrared thermography. *Addit. Manuf.* 24, 595–605.
- Bevans, B., Ramalho, A., Smoqi, Z., Gaikwad, A., Santos, T.G., Rao, P., Oliveira, J., 2023. Monitoring and flaw detection during wire-based directed energy deposition using in-situ acoustic sensing and wavelet graph signal analysis. *Mater. Des.* 225, 111480.
- Cervantes, J., Garcia-Lamont, F., Rodríguez-Mazahua, L., Lopez, A., 2020. A comprehensive survey on support vector machine classification: Applications, challenges and trends. *Neurocomputing* 408, 189–215.
- Chen, T., He, T., Benesty, M., Khotilovich, V., Tang, Y., Cho, H., Chen, K., Mitchell, R., Cano, I., Zhou, T., 2015. Xgboost: extreme gradient boosting. R package version 0.4-2 1, 1–4.
- Chen, Z., Wang, D., Zhang, Y., 2023. Microphone signal specialties in laser powder bed fusion: single-track scan and multi-track scan. *J. Mater. Res. Technol.*
- Cheng, B., Lydon, J., Cooper, K., Cole, V., Northrop, P., Chou, K., 2017. Melt pool dimension measurement in selective laser melting using thermal imaging, 2017 International Solid Freeform Fabrication Symposium. University of Texas at Austin.
- DeRoy, T., Wei, H., Zuback, J., Mukherjee, T., Elmer, J., Milewski, J., Beese, A.M., Wilson-Heid, A., De, A., Zhang, W., 2018. Additive manufacturing of metallic components—process, structure and properties. *Prog. Mater. Sci.* 92, 112–224.
- Drissi-Daoudi, R., Pandiyan, V., Logé, R., Shevchik, S., Masinelli, G., Ghasemi-Tabasi, H., Parrilli, A., Wasmer, K., 2022. Differentiation of materials and laser powder bed fusion processing regimes from airborne acoustic emission combined with machine learning. *Virtual Phys. Prototyp.* 17, 181–204.
- Elliott, D.F., 2013. Handbook of digital signal processing: engineering applications. Elsevier.
- Everton, S.K., Hirsch, M., Stravroulakis, P., Leach, R.K., Clare, A.T., 2016. Review of in-situ process monitoring and in-situ metrology for metal additive manufacturing. *Mater. Des.* 95, 431–445.
- Flandrin, P., Gonçalves, P., Rilling, G., 2004a. Detrending and denoising with empirical mode decompositions, 2004 12th European signal processing conference. IEEE, pp. 1581–1584.
- Flandrin, P., Rilling, G., Gonçalves, P., 2004b. Empirical mode decomposition as a filter bank. *IEEE Signal Process. Lett.* 11, 112–114.
- de Formanoir, C., Hamidi Nasab, M., Schlenger, L., Van Petegem, S., Masinelli, G., Marone Welford, F., Salminen, A., Ganvir, A., Wasmer, K., Logé, R., 2023. Healing of Keyhole Porosity by Means of Defocused Laser Beam Remelting Operando Observation by X-Ray Imaging and Acoustic Emission-Based Detection. Available at SSRN 4516987.
- Goh, G., Sing, S., Yeong, W., 2021. A review on machine learning in 3D printing: applications, potential, and challenges. *Artif. Intell. Rev.* 54, 63–94.
- Gutknecht, K., Cloots, M., Sommerhuber, R., Wegener, K., 2021. Mutual comparison of acoustic, pyrometric and thermographic laser powder bed fusion monitoring. *Mater. Des.* 210, 110036.
- Harake, A., 2022. In-Situ Defect Detection Using Acoustic Vibration Monitoring for Additive Manufacturing Processes.
- Hearst, M.A., Dumais, S.T., Osuna, E., Platt, J., Scholkopf, B., 1998. Support vector machines. *IEEE Intell. Syst. their Appl.* 13, 18–28.
- Ito, K., Kusano, M., Demura, M., Watanabe, M., 2021. Detection and location of microdefects during selective laser melting by wireless acoustic emission measurement. *Addit. Manuf.* 40, 101915.
- Jerri, A.J., 1977. The Shannon sampling theorem—Its various extensions and applications: a tutorial review. *Proc. IEEE* 65, 1565–1596.
- Kanko, J.A., Sibley, A.P., Fraser, J.M., 2016. In situ morphology-based defect detection of selective laser melting through inline coherent imaging. *J. Mater. Process. Technol.* 231, 488–500.
- Khairallah, S.A., Anderson, A.T., Rubenchik, A., King, W.E., 2016. Laser powder-bed fusion additive manufacturing: physics of complex melt flow and formation mechanisms of pores, spatter, and denudation zones. *Acta Mater.* 108, 36–45.
- Kononenko, D.Y., Nikonova, V., Seleznev, M., van den Brink, J., Chernyavsky, D., 2023. An in situ crack detection approach in additive manufacturing based on acoustic emission and machine learning. *Addit. Manuf. Lett.* 5, 100130.
- Koupryanoff, D., Luwes, N., Yadroitsava, I., Yadroitssev, I., 2018. Acoustic emission technique for online detection of fusion defects for single tracks during metal laser powder bed fusion, 2018 International Solid Freeform Fabrication Symposium. University of Texas at Austin.
- Lei, Y., Lin, J., He, Z., Zuo, M.J., 2013. A review on empirical mode decomposition in fault diagnosis of rotating machinery. *Mech. Syst. Signal Process.* 35, 108–126.
- Li, J., Zhang, X., Zhou, Q., Chan, F.T., Hu, Z., 2022. A feature-level multi-sensor fusion approach for in-situ quality monitoring of selective laser melting. *J. Manuf. Process.* 84, 913–926.
- Luo, S., Ma, X., Xu, J., Li, M., Cao, L., 2021. Deep Learning Based Monitoring of Spatter Behavior by the Acoustic Signal in Selective Laser Melting. *Sensors* 21, 7179.
- Mazzoleni, L., Demir, A.G., Caprio, L., Pacher, M., Previtali, B., 2019. Real-time observation of melt pool in selective laser melting: spatial, temporal, and wavelength resolution criteria. *IEEE Trans. Instrum. Meas.* 69, 1179–1190.
- Minhas, A.S., Singh, S., 2021. A new bearing fault diagnosis approach combining sensitive statistical features with improved multiscale permutation entropy method. *Knowl.-Based Syst.* 218, 106883.
- Nasab, M.H., Masinelli, G., de Formanoir, C., Schlenger, L., Van Petegem, S., Esmailzadeh, R., Wasmer, K., Ganvir, A., Salminen, A., Aymanns, F., 2023. Operando X-Ray imaging of stochastic inter-regime instabilities in laser melting processes: direct evidence of acoustic emission signatures.
- Nohara, Y., Matsumoto, K., Soejima, H., Nakashima, N., 2019. Explanation of machine learning models using improved shapley additive explanation, Proceedings of the 10th ACM international conference on bioinformatics, computational biology and health informatics, pp. 546–546.
- Pandiyan, V., Caesarendra, W., Tjahjowidodo, T., Tan, H.H., 2018. In-process tool condition monitoring in compliant abrasive belt grinding process using support vector machine and genetic algorithm. *J. Manuf. Process.* 31, 199–213.
- Pandiyan, V., Drissi-Daoudi, R., Shevchik, S., Masinelli, G., Logé, R., Wasmer, K., 2020. Analysis of time, frequency and time-frequency domain features from acoustic emissions during Laser Powder-Bed fusion process. *Procedia CIRP* 94, 392–397.
- Pandiyan, V., Drissi-Daoudi, R., Shevchik, S., Masinelli, G., Le-Quang, T., Logé, R., Wasmer, K., 2022a. Semi-supervised monitoring of laser powder bed fusion process based on acoustic emissions. *Virtual Phys. Prototyp.* 16, 481–497.
- Pandiyan, V., Drissi-Daoudi, R., Shevchik, S., Masinelli, G., Le-Quang, T., Logé, R., Wasmer, K., 2022a. Deep transfer learning of additive manufacturing mechanisms across materials in metal-based laser powder bed fusion process. *J. Mater. Process. Technol.* 303, 117531.
- Pandiyan, V., Masinelli, G., Claire, N., Le-Quang, T., Hamidi-Nasab, M., de Formanoir, C., Esmailzadeh, R., Goel, S., Marone, F., Logé, R., 2022b. Deep learning-based monitoring of laser powder bed fusion process on variable time-scales using heterogeneous sensing and operando X-ray radiography guidance. *Addit. Manuf.* 58, 103007.
- Parvatharaju, P.S., Doddaiiah, R., Hartvigsen, T., Rundensteiner, E.A., 2021. Learning saliency maps to explain deep time series classifiers, Proceedings of the 30th ACM International Conference on Information & Knowledge Management, pp. 1406–1415.
- Pedregosa, F., Varoquaux, G., Gramfort, A., Michel, V., Thirion, B., Grisel, O., Blondel, M., Prettenhofer, P., Weiss, R., Dubourg, V., 2011. Scikit-learn: machine learning in Python. *J. Mach. Learn. Res.* 12, 2825–2830.
- Redding, M.R., Gold, S.A., Spears, T.G., 2018. Non-contact acoustic inspection method for additive manufacturing processes. Google Pat.
- Rilling, G., Flandrin, P., Gonçalves, P., 2003. On empirical mode decomposition and its algorithms. *IEEE-EURASIP workshop on nonlinear signal and image processing. IEEE, Grado*, pp. 8–11.
- Shevchik, S.A., Kenel, C., Leinenbach, C., Wasmer, K., 2018. Acoustic emission for in situ quality monitoring in additive manufacturing using spectral convolutional neural networks. *Addit. Manuf.* 21, 598–604.
- Shevchik, S.A., Masinelli, G., Kenel, C., Leinenbach, C., Wasmer, K., 2019. Deep learning for in situ and real-time quality monitoring in additive manufacturing using acoustic emission. *IEEE Trans. Ind. Inform.* 15, 5194–5203.
- Snow, Z., Nassar, A.R., Reutzel, E.W., 2020. Invited review article: review of the formation and impact of flaws in powder bed fusion additive manufacturing. *Addit. Manuf.* 36, 101457.
- Tang, B., Dong, S., Song, T., 2012. Method for eliminating mode mixing of empirical mode decomposition based on the revised blind source separation. *Signal Process.* 92, 248–258.
- Tempelman, J.R., Wachtor, A.J., Flynn, E.B., Depond, P.J., Forien, J.-B., Guss, G.M., Calta, N.P., Matthews, M.J., 2022a. Detection of keyhole pore formations in laser powder-bed fusion using acoustic process monitoring measurements. *Addit. Manuf.* 55, 102735.
- Tempelman, J.R., Wachtor, A.J., Flynn, E.B., Depond, P.J., Forien, J.-B., Guss, G.M., Calta, N.P., Matthews, M.J., 2022b. Sensor fusion of pyrometry and acoustic measurements for localized keyhole pore identification in laser powder bed fusion. *J. Mater. Process. Technol.* 308, 117656.
- Wischeropp, T.M., Emmelmann, C., Brandt, M., Pateras, A., 2019. Measurement of actual powder layer height and packing density in a single layer in selective laser melting. *Addit. Manuf.* 28, 176–183.
- Wu, Z., Huang, N.E., 2010. On the filtering properties of the empirical mode decomposition. *Adv. Adapt. Data Anal.* 2, 397–414.
- Ye, D., Hong, G.S., Zhang, Y., Zhu, K., Fuh, J.Y.H., 2018a. Defect detection in selective laser melting technology by acoustic signals with deep belief networks. *Int. J. Adv. Manuf. Technol.* 96, 2791–2801.
- Ye, D.S., Fuh, Y., Zhang, Y., Hong, G., Zhu, K.P., 2018b. Defects recognition in selective laser melting with acoustic signals by SVM based on feature reduction, IOP Conference Series: Materials Science and Engineering. IOP Publishing, p. 012020.
- Zheng, L., Zhang, Q., Cao, H., Wu, W., Ma, H., Ding, X., Yang, J., Duan, X., Fan, S., 2019. Melt pool boundary extraction and its width prediction from infrared images in selective laser melting. *Mater. Des.* 183, 108110.
- Zhirnov, I., Panahi, N., Åsberg, M., Krakhmalev, P., 2022. Process quality assessment with imaging and acoustic monitoring during Laser Powder Bed Fusion. *Procedia CIRP* 111, 363–367.
- Zhou, Z.-H., Zhou, Z.-H., 2021. Ensemble Learning. Springer.